Publications of the Astronomical Society of the Pacific, 132:124501 (22pp), 2020 December https://doi.org/10.1088/1538-3873/abbff3

Development of the MICADO Flat-field and Wavelength Calibration Unit: From Design to Prototyping

Gabriele Rodeghiero[1], Maximilian Häberle[1], Jonas Sauter[1], Miriam Sawczuck[1], Jörg-Uwe Pott[1], Norbert Münch[1], José Ricardo Ramos[1], Vianak Naranjo[1], Wolfgang Kausch[2], Nadeen B. Sabha[2], Enrico Biancalani[1], Santiago Barboza[1], Peter Bizenberger[1], Ralf-Rainer Rohloff[1], Friedrich Müller[1], Ralph Hofferbert[1], Lars Mohr[1], Udo Neumann[1], Ulf Seemann[3], Sebastian Schäfer[4], Kieran Leschinski[5], Oliver Czoske[5], and Werner Laun[1]

[1] Max-Planck-Institut für Astronomie Königstuhl 17 Heidelberg D-69117, Germany; rodeghiero@mpia.de, gabriele.rodeghiero@inaf.it

[2] Institute for Astro- and Particle Physics, University of Innsbruck Technikerstr. 25/8 A-6020 Innsbruck, Austria

[3] ESO Headquarters Karl-Schwarzschild-Str. 2 D-85748 Garching bei München, Germany

[4] Georg-August-Universität Göttingen, Institut für Astrophysik Friedrich-Hund-Platz 1 D-37077 Göttingen, Germany

[5] Institute for Astrophysics, University of Vienna Türkenschanzstr. 17 A-1180 Vienna, Austria

Received 2020 September 8; accepted 2020 October 9; published 2020 November 17

Abstract

We describe the evolution and the analysis of the design that led to the development of the Flat-field and wavelength Calibration Unit (FCU) for the Multi-AO Imaging CAmera for Deep Observations (MICADO) instrument. MICADO will be one of the first light instruments of the Extremely Large Telescope. The FCU challenge in terms of calibration is related to the large size of the MICADO entrance and final focal plane, $\sim$200 mm $\times$ 200 mm. Such a focal plane scale and its segmentation in 3 $\times$ 3 detectors, require significant design modifications with respect to the calibration units of the current and past generation of instruments. The design analysis and ray tracing calculations are complemented with the test and verification of lab prototypes to assess the reliability of the FCU architecture in terms of flat-field illumination uniformity and signal to noise, spectral calibration line coverage and radial velocity stability of the wavelength solution provided to the instrument.

Unified Astronomy Thesaurus concepts: Fabry-Perot interferometers (524); Flux calibration (544)

Online material: color figures

1. Introduction

1.1. The MICADO Instrument

The Multi-AO Imaging CAmera for Deep Observations (MICADO) is one of the first light instruments of the Extremely Large Telescope (ELT). The instrument provides near-infrared (0.8–2.4 μm) high-resolution imaging, relative astrometry, spectroscopy and coronagraphy (Davies et al. 2018). The camera is equipped with two channels: a high-resolution imager covering a Field of View (FoV) of 19″ × 19″ with a 1.5 mas pixel scale, and a low-resolution imager covering a 53″ × 53″ FoV with a 4 mas pixel scale (Schubert et al. 2018). The high-resolution imager will be assisted by a Single-Conjugate Adaptive Optics (SCAO) system (Clénet et al. 2018) that compensates the ground layer at 625 m, while the diffraction-limited capability over the full FoV of the low-resolution imager will be provided by the Multi-conjugate Adaptive Optics RelaY (MAORY). MAORY will enable an MCAO correction mode by means of two post-focal deformable mirrors conjugated at $\sim$5 km and $\sim$12 km height (Diolaiti et al. 2014) in addition to the SCAO mode. The MAORY optics are placed on the Nasmyth platform of the ELT; the MICADO optics are cold and placed in a cryostat that derotates in a gravity invariant configuration underneath the MAORY bench. The ELT focal plane constitutes the MAORY entrance focal plane, and the MAORY output focal plane coincides with the entrance focal plane of MICADO.

1.2. The MICADO Calibration Assembly

The MICADO Calibration Assembly (MCA) provides a suite of calibration functionalities embodied into three subsystems: a Flat-field and wavelength Calibration Unit (FCU), an Astrometric Calibration Unit (ACU) and a Movable source Calibration Unit (MCU) (Rodeghiero et al. 2018).

The MCA is deployed at the MAORY entrance focal plane during the calibration run and retracted during the observations; in this way the light sources and mask are injected as early as possible in the optical train and their light propagates along the same optical path of the science light downstream the ELT focal plane. Generally the calibration unit has to mimic the $F/\#$ of the instrument; the MCA exploits directly the MAORY/relay optics that deliver an $F/17.75$ beam to MICADO without the need of any auxiliary optics. The stray light originated by the FCU is blocked by the MICADO cold stop. The MCA does

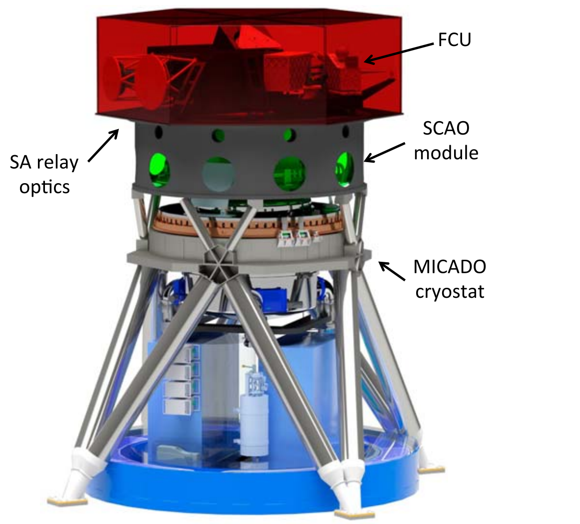

Figure 1. Overview of the MICADO instrument in its Stand-Alone mode for the SCAO observations before the installation of MAORY. The relay optics conveys the light from the ELT down to the MICADO cryostat. The relay optics collects also the light from the MICADO calibration assembly units during the calibration runs.
(A color version of this figure is available in the online journal.)

not need to provide or reproduce a pupil plane. Due to a relative delay of development at the time of writing between the MICADO and MAORY projects, the former has adopted a mitigation strategy to enable early science operations at the ELT only with the SCAO correction and a temporary Stand-Alone Relay Optics. A 3D rendering of the MICADO instrument in its Stand-Alone mode is shown in Figure 1. The latter has the unique function to convey the light from the telescope and the MCA to the instrument (see Figure 2), whereas MAORY will add the MCAO correction. A challenging factor in the realization of the MCA is related to the size of the MICADO focal plane $\sim$200 mm $\times$ 200 mm and its segmentation in 3×3 detectors. The use of conventional integrating spheres to collect and homogenize the light from the calibration sources (te Plate et al. 2005; Wildi et al. 2009; Kelz et al. 2012) is discouraged for their impractical size if rescaled to the MICADO context. The implementation of a dome flat-field strategy (Verdoes Kleijn et al. 2013) is also unfeasible due to the size of the ELT (39 m diameter).

1.3. The Flat-field and Wavelength Calibration Unit

The FCU overcomes this problem relying on an ensemble of miniaturized halogen lamps coupled with a Spectralon panel that is the material with the best diffusing Lambertian properties over ultraviolet, visible, and near-infrared range (Bhandari et al. 2011). The spatial uniformity of the flat-field pattern is accurately studied with a full-scale replica of the FCU both at small and large (full FoV) scales. The FCU provides also the wavelength calibration sources for the MICADO echelle spectrograph that has an intermediary resolution of $14{,}000 < R < 20{,}000$. The current baseline is based on 4 gas lamps (Ar, Xe, Ne, Kr) already in use in the X-shooter instrument (Kerber et al. 2008), plus a K band Fiber-based Fabry–Pérot (FFP) to supply the progressive lack of bright natural gas lines beyond $\sim$1.8 μm. The design description of the FCU is reported in Section 2, the results of the flat-field illumination uniformity and signal-to-noise ratio (S/N) measurements are collected in Section 3. The wavelength calibration sources in terms of line coverage of the echellogram orders, Radial Velocity (RV) stability and opto-mechanical interfaces are discussed in Sections 4 and 5. In the final paragraph 6 we simulate a typical calibration spectrum with the MICADO spectroscopic pipeline under development for the instrument operations.

2. Flat-field and Wavelength Calibration Unit—FCU

The MICADO FCU has four main functionalities:

(i) provide a flat-field calibration by means of a light source with spectral continuum and suitable S/N, for a 2–120 s exposure, to trace the detector response in terms of quantum efficiency and pixel to pixel variations; The flat-field uniformity shall be $\geqslant$90% over the full MICADO FoV (53″) and $\geqslant$99.9% over 1″.
(ii) map the hot/dead pixels and vignetting factors.
(iii) detect nonlinearity effects of the detector down to 1% of its dynamic range.
(iv) provide an average of 10 calibration lines with suitable S/N and with a Radial Velocity stability of minimum 0.3 km s^{-1} for each order of the echellogram and detector to calibrate the wavelength response of the instrument spectrograph.

2.1. The Need for a New Concept Design

Many of the instruments operating in the 8 m class telescopes rely on Integrating Spheres (IS) to achieve the flat-field calibration (te Plate et al. 2005; Wildi et al. 2009; Kelz et al. 2012). An IS homogenizes the injected light by multiple Lambertian scattering processes and reflections onto the spherical walls of its cavity that are coated with highly reflective material (Spectralon). Some instruments, alternatively or complementary to the IS, perform periodic flat-field calibration on sky at twilight (Chromey & Hasselbacher 1996; Wei et al. 2014) and dome flat-fielding (Verdoes Kleijn et al. 2013). Both the IS and the dome flat-fielding can hardly be applied to MICADO. The large linear size of the instrument Focal Plane Array (FPA) of MICADO, $\sim$200 mm $\times$ 200 mm, constitutes the main challenge for the use of an IS that would be impractically large. The uniformity of the IS output can be described mathematically with some simple relations between the diameter of the sphere and that of its input and exit ports. A good rule of thumb (Labsphere 2017; Photonics 2020)

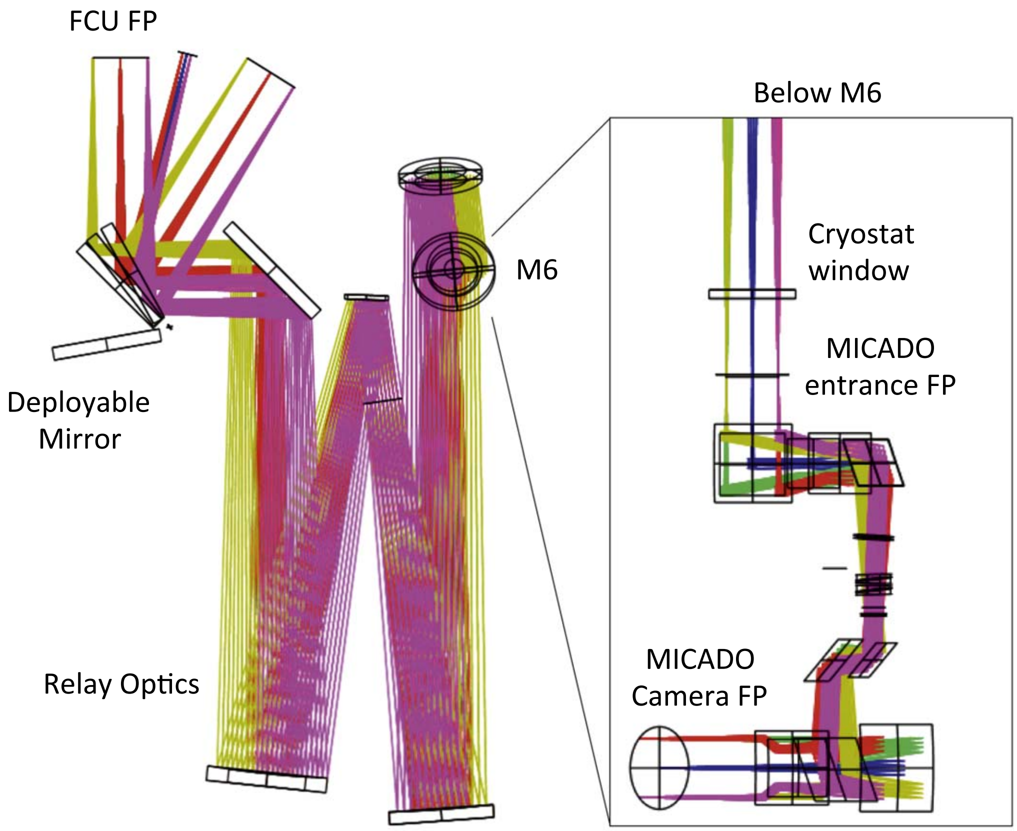

Figure 2. The light from the FCU focal plane is conveyed via a deployable mirror into the relay optics (left) that relays it to the MICADO entrance and camera focal planes (right).
(A color version of this figure is available in the online journal.)

provided by IS manufacturers from empirical performance studies, suggests to contain the fraction loss of the IS reflecting area due to the input (lamps) and exit ports (output focal plane) within $2\% < f_{\text{loss}} < 5\%$ as reported in Equation (1):

$$f_{\text{loss}} \sim \frac{2\pi h r_{\text{exit port}} + \pi r_{\text{input port}}^2}{4\pi r_{\text{IS}}^2} \leqslant 5\% \tag{1}$$

considering the exit port as a spherical cap of height h and the input port small enough to be assumed flat and circular. The factor f_{loss} needs to be minimized because the IS radiance has an hyperbolic drop with its increase (Labsphere 2017; Photonics 2020). The second rule of thumb suggests that to achieve a good (∼98%) spatial uniformity of the illumination pattern at the exit port, the diameter of the IS should be at least 3 times larger than its exit port (Labsphere 2017). Neglecting the dimming problem, the best uniformity would be attained with a large IS and a small exit port. The application of these requirements to MICADO, with a diameter of the FPA ø ∼ 280 mm, traduces in having an IS with a minimum diameter of ø ∼700 mm that requires a volume envelope not available in the instrument and that would turn significantly dimmer the calibration light sources. Although instruments like OmegaCAM with even bigger focal planes exist (∼240 mm × 240 mm) and they rely on dome flat-fielding to overcome this limitation, the size of the ELT is prohibitively large to enable this approach for MICADO. To overcome these major design issues, two alternative design options of the FCU have been proposed and studied as described in the next section.

2.2. FCU Design Evolution

The first FCU assessed design combines the use of a small IS coupled with a large Spectralon panel deployed at the instrument entrance focal plane as discussed in Rodeghiero et al. (2018). In this configuration the flat-field lamp and the gas lamps for the wavelength calibration are placed inside the IS that homogenizes their light. At the exit port a flat pick off mirror redirects the light toward the Spectralon panel that has the same size as the instrument focal plane. This design overcomes the problem of a large IS although the light sources are significantly dimmed by the two stage scattering process (IS + Spectralon). Subsequent developments of the MAORY and MCA opto-mechanical interface have led to the design of a

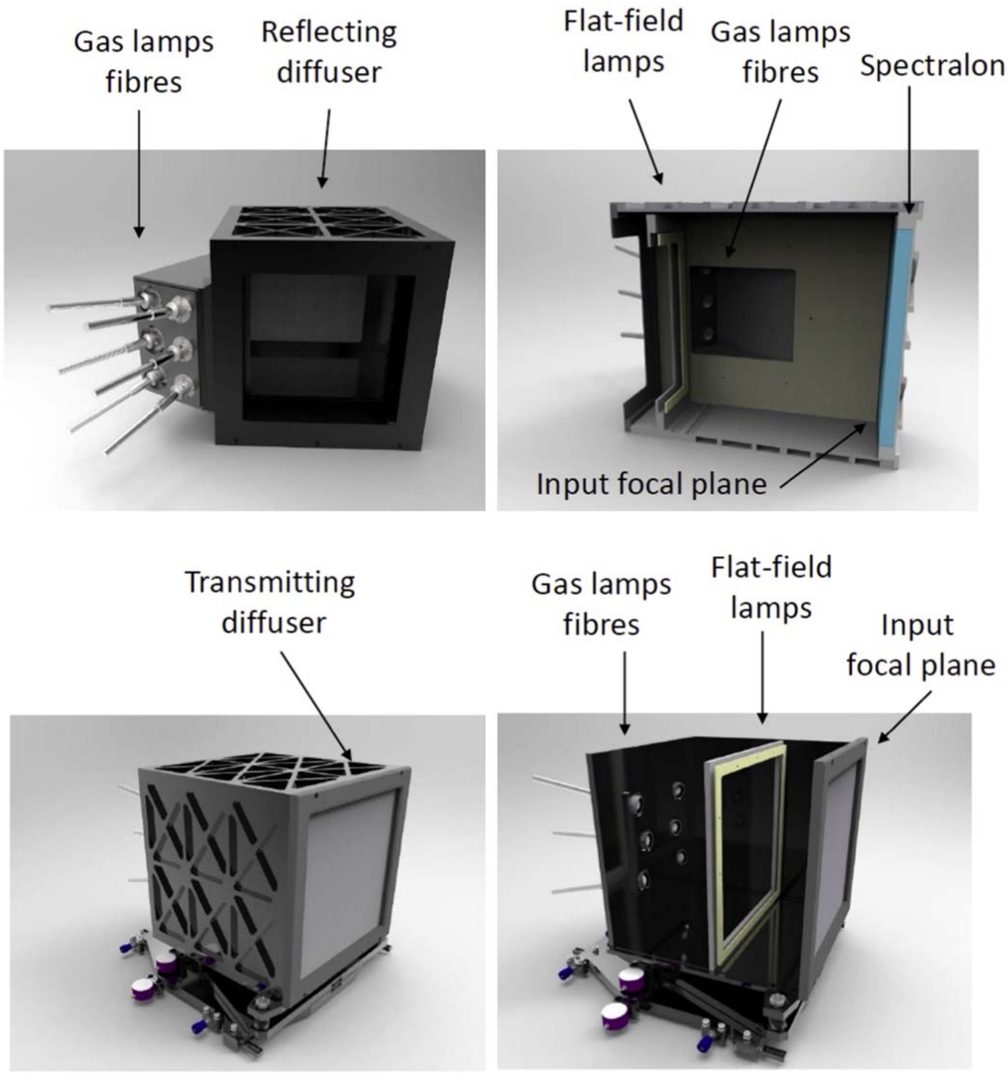

Figure 3. Left: top: the MICADO Flat-field and wavelength Calibration Unit (FCU) in reflecting mode collects and diffuses by means of a Spectralon panel (aquamarine) the light from twenty miniaturized halogen lamps (not visible) and four gas lamps plus a Fibre Fabry–Pérot (FFP). The gas lamps and the FFP are external to the unit and fed by the fiber bundles plugged on the left side of the unit. This design configuration is utilized for the standalone phase of MICADO. Bottom: FCU design in transmitting mode with the thin diffuser developed to be compatible with the latest MAORY design; the diffuser is installed at the exit baffle of the original FCU and deployed at the ELT focal plane. The gas lamps fiber bundles are plugged from behind the unit at the opposite side of the diffuser.
(A color version of this figure is available in the online journal.)

common elevator to deploy the MCA and the MAORY calibration unit at the instrument entrance focal plane (Rodeghiero et al. 2018) where the limited allocated volume for the MCA required a significant shortening of the FCU baffle. Since the scattering efficiency of the Spectralon degrades heavily for Angle of Incidence (AoI) larger than $\sim 40^{\circ}$ (Bhandari et al. 2011), a shortening of the FCU baffle with an off-axis position of the IS was no longer possible. The design has been modified removing the IS and the pick off mirror while leaving the Spectralon panel as single diffuser (Figure 3-top). This design is labeled as FCU reflecting mode. The initial 10 W halogen lamp for the flat field calibration has been replaced with an ensemble of 20 miniaturized ($\sim$0.5 W each, $\sim$2 mm bulb) halogen lamps (MGG-4115-09) connected in parallel and mounted on a frame facing the Spectralon panel as shown in Figure 4. The gas lamps light for the wavelength calibration is conveyed and projected onto the Spectralon panel via optical fibres from a series of external boxes containing the lamps as discussed in Section 4.

The MAORY design underwent several changes along its development path (Lombini et al. 2019). Currently (mid 2020) the MAORY design includes a Corrective Refractive Plate

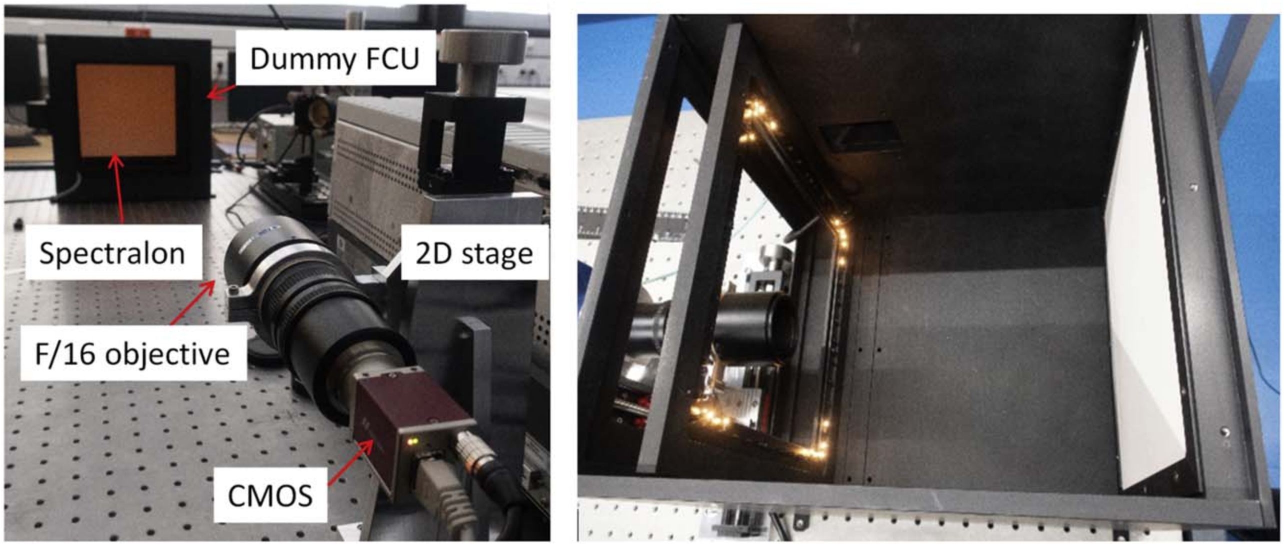

Figure 4. Left: lab setup for the measurement of the flat-field spatial uniformity: the Spectralon panel of the FCU replica is reimaged with an $f/16$ objective lens to a CMOS camera that can patrol the whole area of the panel by a 2D manual stage. Right: insight view of the FCU with the array of miniaturized halogen lamps arranged at the corners of the FCU to maximize the uniformity of the flat-field pattern.
(A color version of this figure is available in the online journal.)

(CRP) about 350 mm away from the ELT focal plane. In this scenario the FCU would physically collide with the CRP when deployed, requiring additional design modifications. The solution adopted exploits the same FCU architecture shown in Figure 3-top with the addition of a transmitting thin diffuser installed at the termination of the baffle unit (FCU in transmitting mode). In this configuration the FCU is moved backward with respect to its nominal position in the elevator such that the transmitting diffuser is deployed in correspondence of the ELT focal plane. The original FCU architecture and illumination system are preserved, while two additional diffusing elements are installed in front of it (Figure 3-bottom): a 250 μm Zenith Polymer Membrane (ZPM) diffuser with a 25% gray transmission profile within the MICADO wavelength range and a sandblasted glass plate. The current baseline of the MICADO project relies on the FCU in reflecting mode for the instrument standalone mode and in transmitting mode for the MAORY mode. In the next paragraph we report the flat-field uniformity study carried out for both the designs of the FCU, reflecting and transmitting.

3. Flat-field Uniformity and S/N

The flat-field spatial uniformity and its stability over time is of central importance for the calibration of the FPA. This functionality needs to provide a fast (2–120 s) and suitable S/N calibration in all the instrument filters. A replica of the FCU, has been built in house to analyze the spatial uniformity of the flat-field pattern and to estimate the S/N within typical calibration exposure times for both the reflecting and transmitting modes. As part of the development we also assessed the temporal stability of the light sources on a short ($\sim$minutes) and long ($\sim$month) term by intensive duty cycles (paragraph 3.2). The setup to measure the flat-field uniformity as delivered to the instrument entrance focal plane is shown in Figure 4 and it is the same both for reflecting and transmitting modes.

The Spectralon panel and the transmitting membrane panel are re-imaged with an $f/16$ objective lens (Navitar Zoom 7000) to a CMOS camera (Allied Vision Mako G-319, 400–1000 nm) that can tangentially patrol the full panel area by means of a 2D manual stage. The uniformity has been measured also with a near-infrared (NIR) camera (Xenics Xeva-1.7-320, 900–1700 nm) finding no significant differences or color dependence of the former with the wavelength. To account for the camera artifacts like pixel-to-pixel variations, dust on the sensor and lens, and vignetting factors a master flat of the camera has been produced by retrieving a series of dithered images of the Spectralon surface.

3.1. Flat-field Spatial Uniformity

The spatial uniformity of the FCU pattern is measured both over the full FoV and at small spatial scales ($1''$). The MCA flat-field uniformity requirement is respectively $\geqslant$90% over the full MICADO FoV ($53''$) and $\geqslant$99.9% over $1''$. To achieve a sufficient robustness against statistical uncertainty (e.g., photon counting shot noise), 100 frames are combined and the median is taken. An initial attempt driven by an intuitive approach led us populating the entire lamps frame (48 sources) as shown in

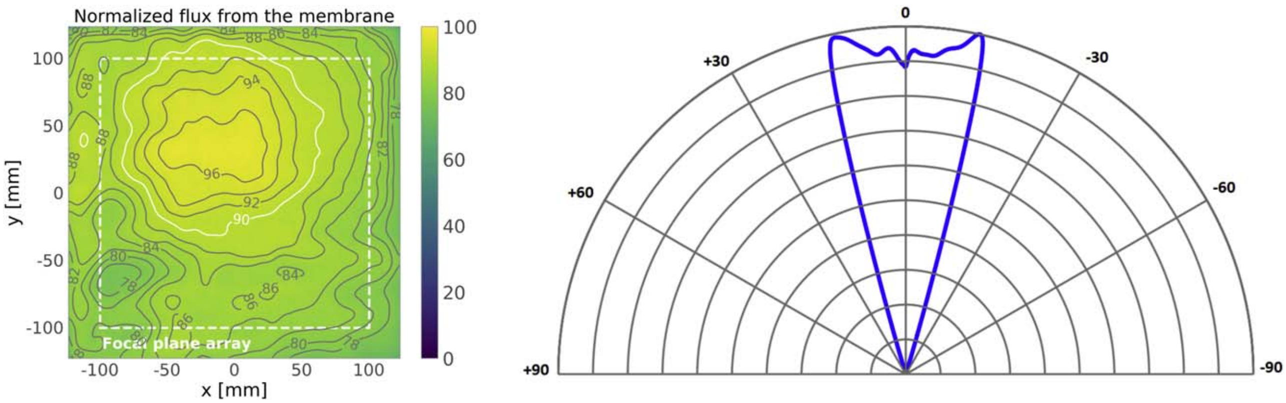

Figure 5. Left: measurement of the illumination pattern from a single lamp from the FCU in transmitting mode. Right: reconstructed cross-section profile (Zemax) of a single lamp, the beamwidth is $\sim 30°$.
(A color version of this figure is available in the online journal.)

Figure 6-right. This configuration does not satisfies the full field uniformity requirements as the reader can observe in Figure 6-left. The explanation lays in the bore-sight emission angles of the single lamps that overlap in the center of the focal plane building up an excess of flux. From the measurement of the illumination pattern of a single lamp and the FCU geometry we derive a core beamwidth of approximately 30° (Figure 5).

The optimal lamps configuration has been therefore determined by mapping the illumination footprint of a single lamp at the FCU focal plane and by numerically simulating the flat-field pattern from different geometric lamps ensembles (Figure 7). The ultimate fine tuning has been achieved in the lab by adding-removing the lamps from the support frame given some limitations in the fidelity of modeling the Spectralon bidirectional scattering distribution function. The highest spatial uniformity in reflecting mode is found for an arrangement of 20 miniaturized flat-field lamps distributed at groups of five at each corner of the FCU. The measured uniformity of the flat-field over the whole FoV is equal or higher than 90% matching the performance requirement of the MCA (as shown in Figure 8).

The variability between the individual lamps and subsequently to a lamp replacement affects the global uniformity at 1%–2% level. We also assessed that the failure of one lamp in a certain corner or of two lamps on different corners is tolerable since it does not deteriorate the flat-field uniformity below the 90% level (Figure 9). The failure of two lamps at the same corner makes the homogeneity falling below 90%. The lamp failure is clearly observable with an InGaAs photodiode that detects a $\sim$3% decrement of its photocurrent for every lamp removed. The pattern uniformity does not show any strong dependence on the lamps input voltage (lamp flux).

Also the initial attempts for the FCU in transmitting mode were not compliant with the uniformity requirements. The intuitive idea of populating a full matrix of lamps placed directly behind the ZPM led to the pattern shown in Figure 10. As for the initial configuration of the FCU in reflecting mode (Figure 6) the bore-sight emission angles of the single lamps overlap in the center of the focal plane accumulating an excess of light flux. The architecture has been therefore oriented toward a similar configuration for the FCU in reflecting mode (8). The use of a lamp frame instead of a filled matrix leads also to the advantage of placing the input ports for the gas lamps fibres directly behind the ZPM instead of in a off-axis configuration as in the reflecting mode.

The highest uniformity in transmitting mode, fulfilling the requirement, is achieved with the same lamps configuration of the reflecting FCU with the addition of 4 lamps, each one in the middle of the four FCU edges (Figure 11).

At 1″ scale the uniformity requirement is higher (99.9%) and more difficult to achieve: the local defects of the Spectralon panel and the intrinsic granularity texture of the fluoropolymer material at $\sim$150 μm scales lead to a deterioration of the pattern uniformity. In this measurement the imaging system is positioned at a separation from the Spectralon panel such that the same pixel scale of the MICADO detector (15 $\mu\mathrm{m\,px}^{-1}$) is achieved. The local flat-field at 1″ FoV is assessed in different positions of the FoV as shown in Figure 12-left. The pattern uniformity with respect to the median value of the frame is between $p_5 \sim 99.3\%$ and $p_{95} \sim 100.7\%$, with p_5 quantile at 5% of the data distribution. A way to improve the uniformity is shifting the Spectralon panel from the entrance focal plane of the instrument by different offsets ($\delta_{\mathrm{FP}} = \pm 20$ mm). We retrieved from Zemax the size of the defocused PSF on the MICADO detector for different defocus ranges of the entrance focal plane. The effect of the Spectralon focus offset is simulated applying to the measured flat-field maps a Gaussian filter with a Full Width Half Maximum (FWHM) equal to the diameter of the defocused PSF (Figure 12-right).

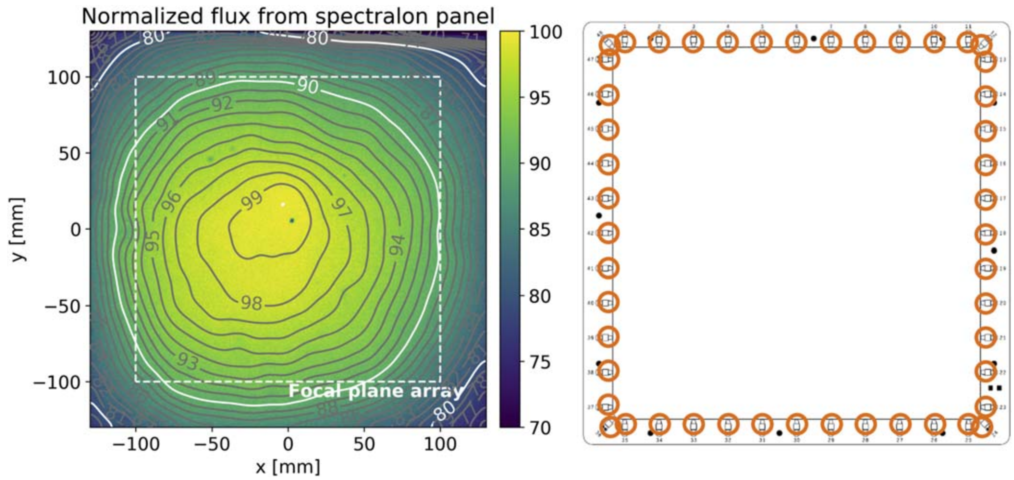

Figure 6. Left: measured flat-field uniformity for the FCU prototype in reflecting mode for the first attempt with the lamps frame fully populated. Right: all the 48 lamps are active (orange circles).
(A color version of this figure is available in the online journal.)

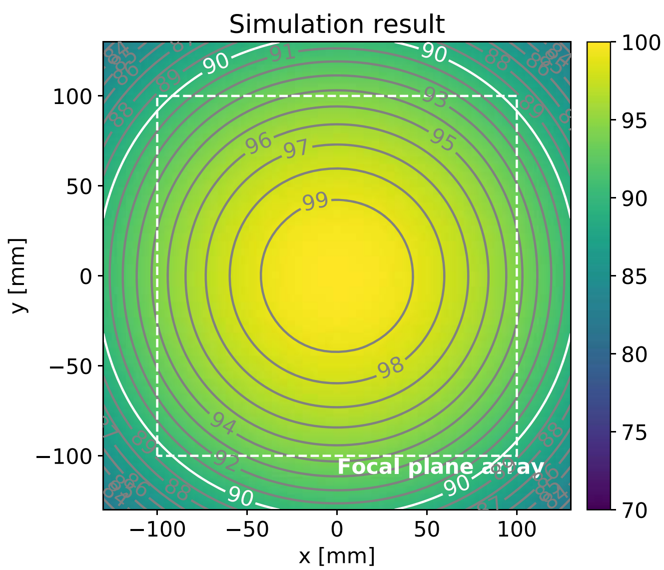

Figure 7. Simulation of the flat-field illumination pattern over the full MICADO FoV obtained positioning 5 lamps at each corner of the FCU.
(A color version of this figure is available in the online journal.)

The non-uniformity pattern obtained through the convolution with the defocused caustic leads to an rms of ∼0.1% and a *PV* of 0.5%, improving sensibly the local uniformity and reaching at rms level the flatness requirement over 1″ FoV. The same measurements and analysis are repeated for the FCU in transmitting mode leading to the results reported in Figure 13. The local uniformity is non-comformant due to some local thinning of the ZPM texture at typical scales of 50–130 μm. The problem has been mitigated by adding in front of the ZPM a ground glass diffuser (model SQ-120 grit from EO), at the expenses of longer calibration times to reach the same S/N. The local non-uniformities have been reduced to an rms of ∼0.3% as shown in Figure 14. The residual deviation from the 99.9% uniformity shall be assessed with the final instrument setup that could be even more sensitive to defocus thus leading to a higher uniformity for any $\delta_{\rm FP}$ of the FCU from the nominal focal plane position. In case the local non-uniformities cannot be suppressed beyond 0.3% the impact on the instrument calibration does not seem to compromise the instrument performance and the quality of the data.

3.2. Flat-field S/N and Stability

Another important requirement for the flat-field calibration is the time duration: to avoid large calibration overhead the goal is to keep the exposure between 2 s for the broad-band filters and 120 s for the narrower. The minimum Detector Integration Time (DIT) depends on the detector readout electronics and for the HAWAII-4RG detectors is ∼2 s. The broad-band filters like H and K saturate quickly and they require the shortest DIT available, whereas the narrow-band require longer exposure times suggesting the use of two illumination levels for the FCU depending on the filter in use. To assess this functionality, we measured the flat-field radiance and its translation in S/N at the instrument focal plane. The radiance is measured empirically while the propagation from the FCU downstream to the MICADO focal plane is done numerically taking into account the optical system throughput. The lab setup is based on two calibrated InGaAs photodiodes (SM05PD4B, G12183-003K) alternately coupled with a Keithley 6430 source meter for the signal acquisition. The G12183-003K has a responsivity extending to 2.5 μm and it is used to probe the lower limit of illumination of the FCU. An auxiliary collimating lens focuses

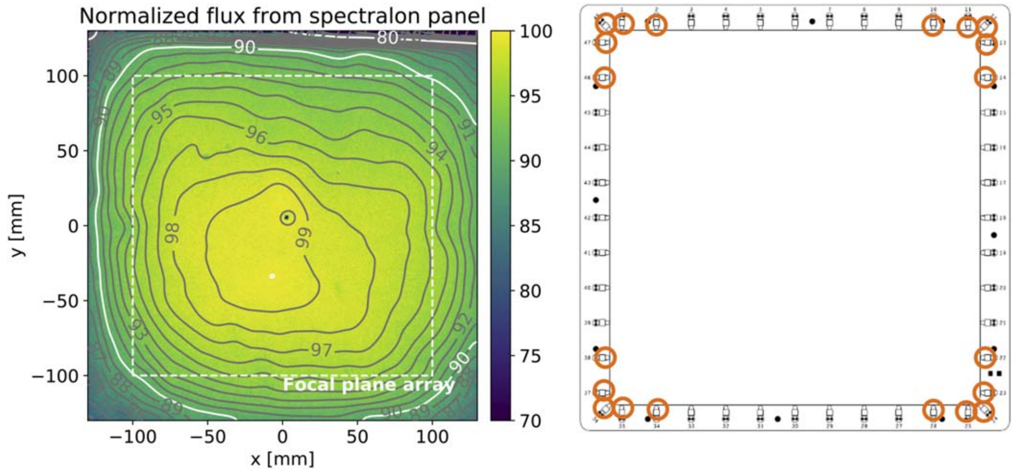

Figure 8. Left: measured flat-field uniformity for the FCU prototype in reflecting mode shown in Figure 3-top with the contour line of 90% (MCA requirement) in white. Right: configuration of the active lamps in the orange circles.
(A color version of this figure is available in the online journal.)

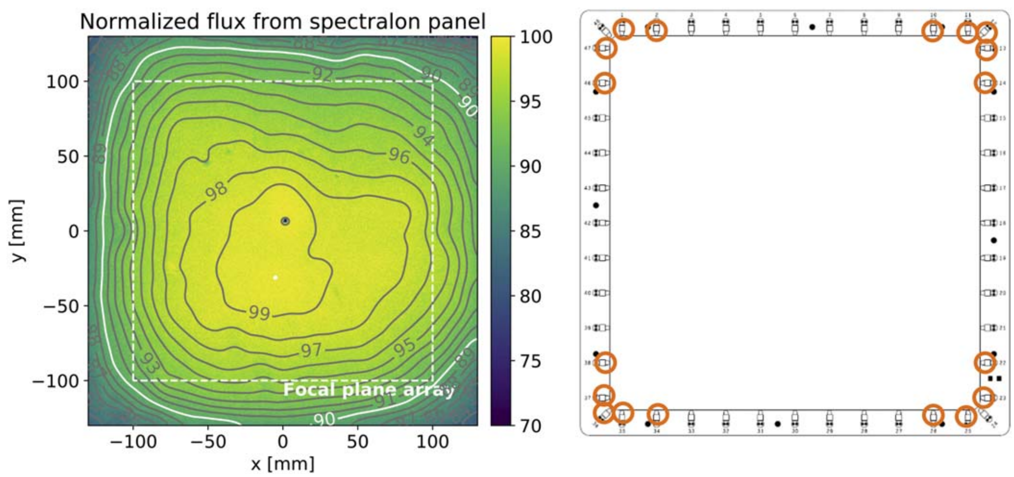

Figure 9. Measured flat-field uniformity for the FCU prototype in reflection mode with 2 lamps missing at opposite corners (top-left and bottom-right) as to simulate a failure.
(A color version of this figure is available in the online journal.)

the light from the Spectralon panel onto the sensitive area of the photodiode. The flux reaching the sensitive area of the photodiode is $\Phi = t \cdot A\Omega \cdot L_\lambda$, being t the product of the lens transmission and the photodiode responsivity, L_λ the Spectralon radiance and the factor $A\Omega$ the system etendue. The etendue is a geometric factor and it is the product of the photodiode sensitive area and the solid angle subtended by the latter at the Spectralon panel. The radiance of the Spectralon $L_\lambda = C(I) \cdot B_\lambda(T_{\mathrm{lamp}})$, is the product of a function of the measured current $C(I)$ from the photodiode and the Blackbody (BB) temperature directly related to the lamp filament temperature. To determine the latter quantity, we used a four-wires low parasitic current circuit that led to measure the filament resistance $R(T)$. Subsequently the resistance is converted into BB temperature at different input voltage as described by Equation (2).

$$T_{\mathrm{BB}} = \frac{1}{\alpha_W}\left(\frac{R(T)}{R(300\ \mathrm{K})} - 1\right) + 300\ \mathrm{K} \tag{2}$$

with α_W being the temperature coefficient of the Tungsten. Equation (2) is derived by expressing the standard textbook formula of the linear thermal expansion law $R(T) = R_0(1 + \alpha(T - T_0))$ in terms of T. Once L_λ is measured empirically, it is propagated numerically to the MICADO

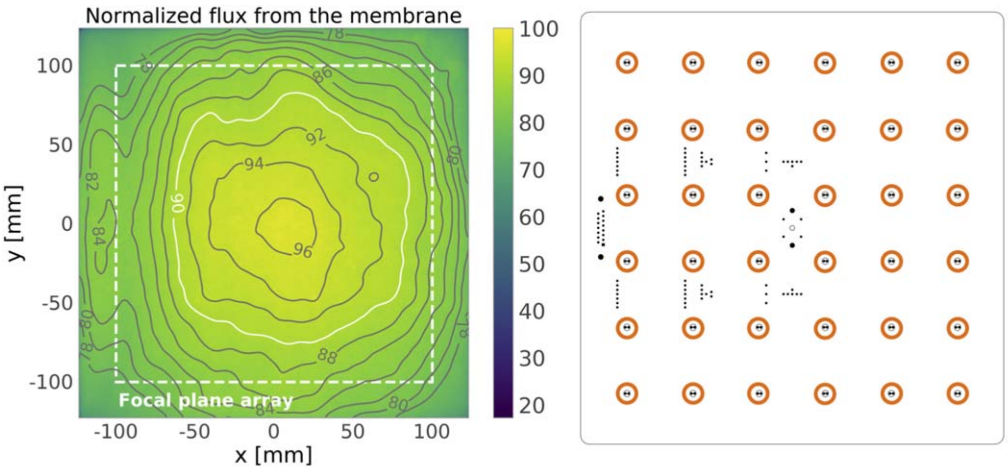

Figure 10. Left: measured flat-field uniformity for the FCU prototype in transmitting mode for the first attempt with a full matrix of lamps (right).
(A color version of this figure is available in the online journal.)

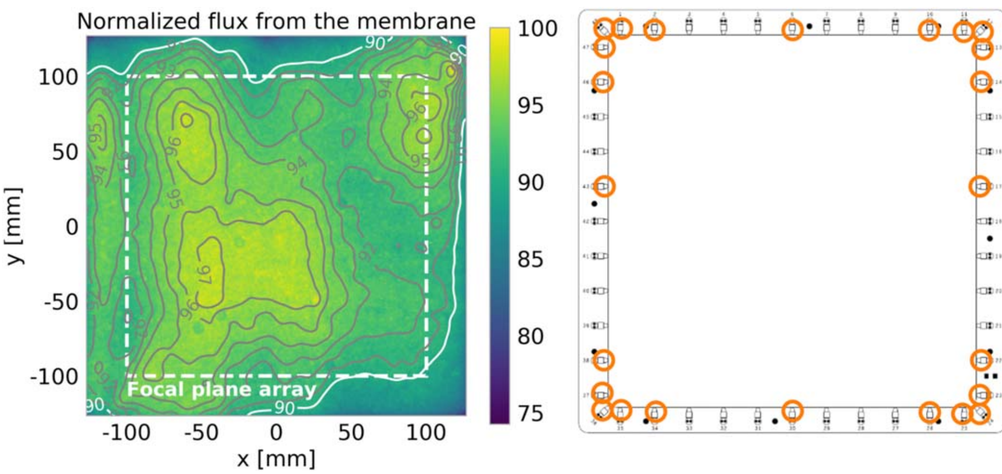

Figure 11. Measured flat-field uniformity for the FCU prototype in transmitting mode (Figure 3-bottom) with the contour line of 90% in white. Right: configuration of the active lamps in the orange circles.
(A color version of this figure is available in the online journal.)

focal plane and converted into a photons rate:

$$S_\gamma = \mathrm{DIT} \int_{\lambda_1}^{\lambda_2} \frac{A\Omega(F/\#) \cdot QE \cdot \epsilon \cdot L_\lambda \cdot \lambda \cdot d\lambda}{h \cdot c} \tag{3}$$

with $A\Omega(F/\#)$ being the etendue of the MICADO instrument, QE the detector quantum efficiency, ϵ the overall optical transmission of MAORY + MICADO; the signal is integrated between the cut-off wavelengths $[\lambda_1, \lambda_2]$ of the filter considered. Equation (3) represents one of the most common formulations for the estimate of the number of photons reaching the focal plane of an astronomical telescope/instrument (Rico et al. 2012) To calculate the S/N we assume typical values for dark current (0.05 e^- s^{-1}), readout noise (25 e^-) and full well capacity (150,000 e^-) of the HAWAII-4RG (Loose et al. 2007; Hall et al. 2016) combined in quadrature with the Poissonian noise:

$$\mathrm{S/N}_\gamma = \frac{S_\gamma \cdot \mathrm{DIT}}{\sqrt{S_\gamma \cdot \mathrm{DIT} + \mathrm{Dark} \cdot \mathrm{DIT} + \sigma^2_{\mathrm{RON}}}}. \tag{4}$$

The results of the expected S/N are shown in Figure 15 (Bottom): a suitable calibration within 2 s and 120 s is possible with two different input voltages, ∼1 V for filters bluer than J and for narrow band filters in general (up to 120 s), and ∼0.6 V for H and K band filters (up to 2 s).

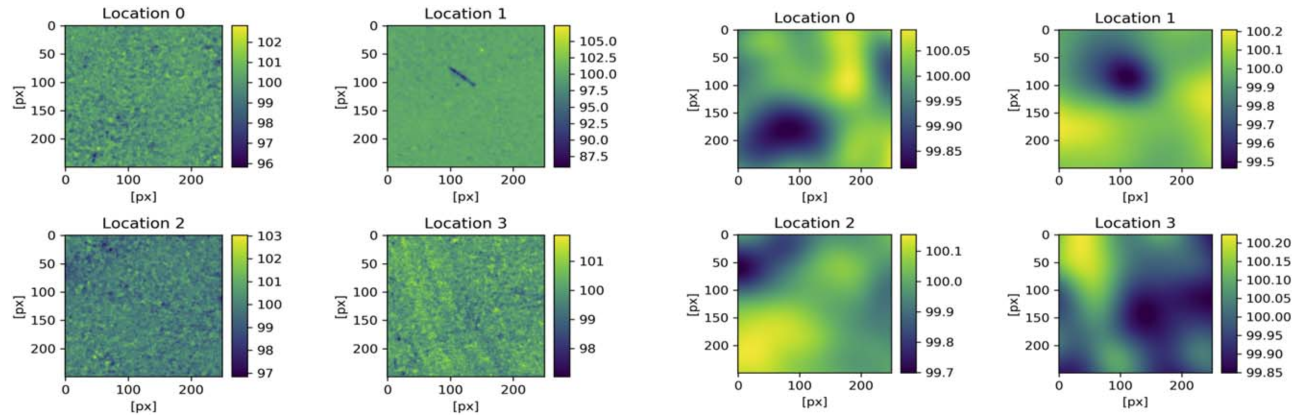

Figure 12. Left: the measured flat-field at 1″ scale shows a spatial uniformity between $p_5 \sim 99.3\%$ and $p_{95} \sim 100.7\%$. Right: a pattern uniformity of ∼99.9% (rms) can be obtained by off-setting by ∼20 mm the Spectralon panel with respect to the entrance focal plane of the instrument.
(A color version of this figure is available in the online journal.)

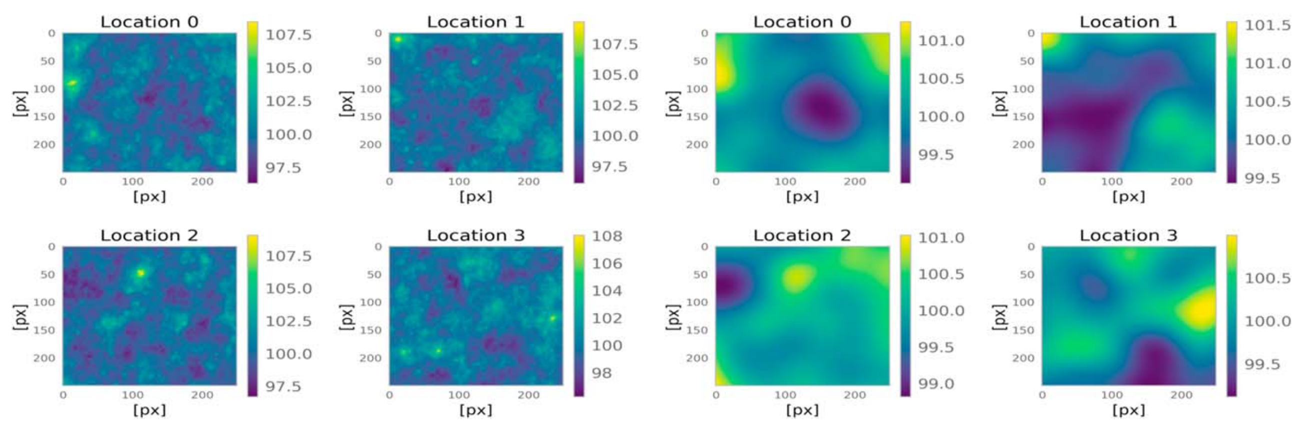

Figure 13. Left: measured flat-field at 1″ scale with a 250 μm membrane. Right: the pattern uniformity with a 20 mm defocus is still not compliant with the ∼99.9% requirement.
(A color version of this figure is available in the online journal.)

Figure 15 (Top) shows also the capability of the FCU to provide a light signal down to 1% of the detector dynamic range for conducting nonlinearity studies of the latter. The last feature of the flat-field lamps analyzed is their stability and reliability over time. The short and long term stability of the lamp flux has been monitored using the above mentioned photodiode with lamp enclosed in a light-tight barrel and operated for a month with the duty cycle: 30 minutes on—5 minutes off. The measured flux stability on short term (30 minutes) is $\Delta F < 0.004\%$ rms with a PV of 0.02%; the long term stability (1 month) is $\Delta F < 0.07\%$ rms with a PV of 0.42% without any active control of the temperature of the barrel (see Figure 16). The rms and PV values are calculated excluding the warm-up phase of the lamps. The measurements are corrected by dark current of the photodiode retrieved by the temperature sensor data. The average lifetime of the lamps is 10,000 hr.

4. Wavelength Calibration Strategy

The wavelength calibration of the astronomical spectrographs is achieved by means of different absolute calibrators, e.g., gas lamps (Kerber et al. 2008), telluric lines (Seemann et al. 2014), Laser Frequency Comb (LFC) (Hänsch 2006), and relative calibrators like Filter/Fibre Fabry–Pérot (FFP) (Huke et al. 2018). While LFCs represent the ideal calibrator providing an equally spaced, uniformly bright and absolute comb of lines, their cost is still relatively high although alternative solutions based on different technologies as the ring resonators are emerging (Boggio et al. 2012). The cheapest solutions, gas lamps and telluric lines, suffer from non-uniform distribution of the lines along the spectrum and unbalanced brightness between different lines; the latter are subjected also to non-constant intensity depending on the atmospheric conditions. The FFP stands in between the gas lamps and the LFC providing an equally spaced and uniformly bright comb of

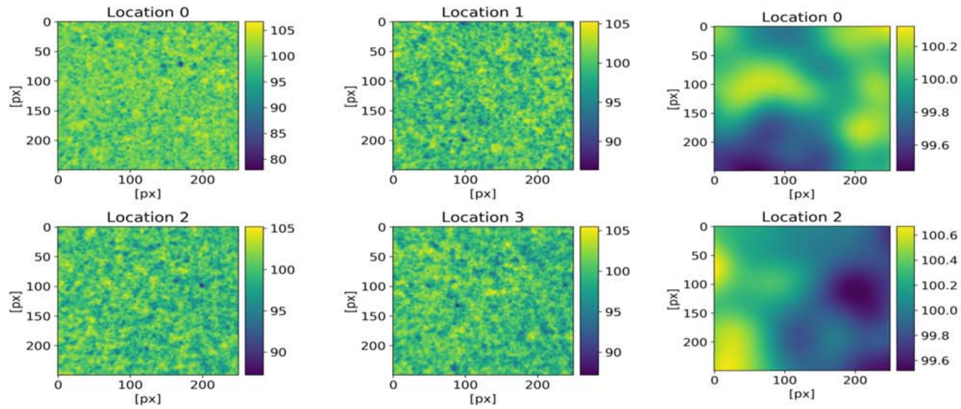

Figure 14. Left: measured flat-field at 1″ scale with a ground glass diffuser placed in front of the ZMP. Right: the residual non-uniformities for a 20 mm defocus of the FCU focal plane are at 0.3% rms level.

(A color version of this figure is available in the online journal.)

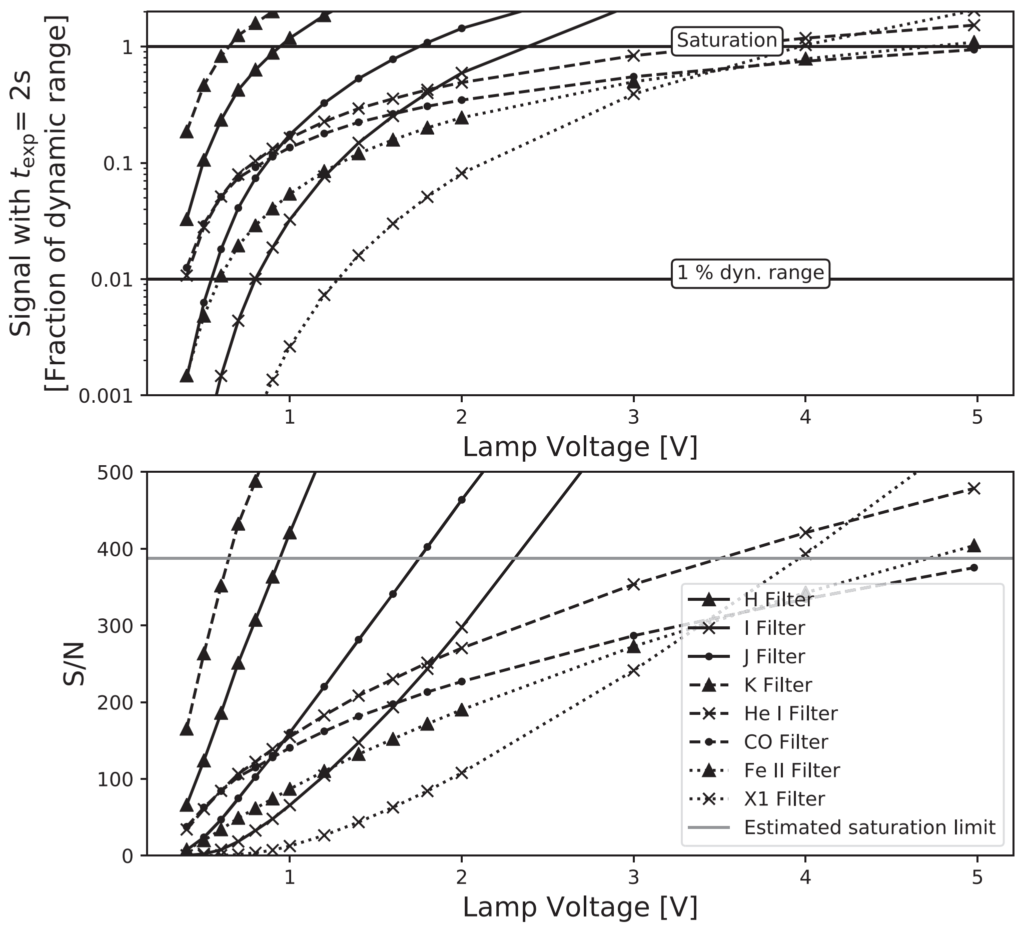

Figure 15. Top: the tuning the lamps voltage supply allows to scan the detector dynamic range down to the 1% scale. The lower limit enables the detection of nonlinearity effects of the detector. Bottom: S/N estimates for different filters and lamp supply voltages at a fixed exposure time of 2 s (minimum DIT). Saturation limit at 150,000 e^{-}.

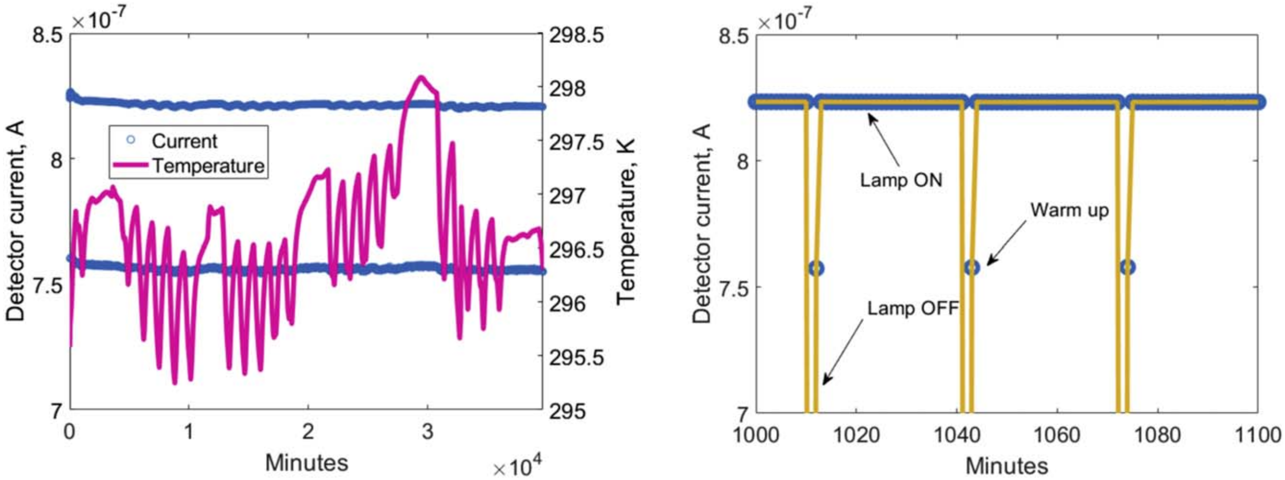

Figure 16. Left: long term stability (1 month) of FCU lamps with 1 minutes sampling. Right: short term stability (30 minutes—calibration run). The lower row of flux points show the warm-up time of the lamps (1 minutes). The detector signal has been corrected for dark current derived from the temperature measurement (pink). The long and short term stability is calculated excluding the warm-up phase of the lamp.
(A color version of this figure is available in the online journal.)

lines, but it does not offer an absolute wavelength calibration since its lines can drift with temperature and pressure changes. The most common gas lamps in use in the current generation of NIR instruments are Kr, Xe, Ar, Ne (Kerber et al. 2008) but they all suffer a progressive decrease of line density beyond 1.8 μm leading to a weaker wavelength solution in K band. MICADO is equipped with an echelle spectrograph of intermediary resolution $14{,}000 < R < 20{,}000$ optimized for the observation of compact objects. The orders extend between the 3rd (K band) and the 8$^{\text{th}}$ (I band). The instrument can deploy three different slits (Davies et al. 2018): s1 = 15 as × 20 mas, s2 = 3 as × 16 mas and s3 = 3 as × 48 mas. Although the resolution is not extreme and high precision RV studies are not among the science goals of the MICADO spectroscopy, the segmentation of the focal plane (3×3 detectors, see Section 6) and the thermal drift within the cryostat (0.1 K/h) add an additional challenge to the calibration. The most reliable approach is deriving and building a dedicated wavelength solution for each detector to be linked between adjacent detectors. To do so, a minimum of ten suitable calibration lines per order, per detector shall be available. For these reasons, in addition to the Ne, Xe, Ar and Kr lamps we choose to implement a K band FFP. The FFP or etalon, is a light resonant cavity. The light is injected into the filter with a certain angle and it is reflected back and forth multiple times such that only the normal modes of light into the cavity survive and are transmitted. The cavity is generally realized putting in close separation two air-spaced/glass-spaced, or evacuated, wedged and polished surfaces. The surfaces are coated to achieve a certain reflectance R that determines the finesse, $F = \pi\sqrt{R}/(1 - R)$. The finesse is a measure of the number of reflections within the cavity and higher F leads to more peaked and narrow lines. The finesse regulates also the separation between the lines, the Free Spectral Range (FSR), by the relation $F = \mathrm{FSR}/\mathrm{FWHM}$; Most of the FFP are installed in a vacuum vessel to achieve the required temperature and pressure stabilization (Schäfer et al. 2018). Alternative designs rely on a Single Mode Fiber (SMF) cavity as described by Halverson et al. (2014). The cavity is made of two SMF coated with a dielectric and surrounded by a ferrule to keep them aligned and equipped with a thermistor and a thermoelectric cooler (TEC) to stabilize its temperature. The whole FFP has the size of a lighter as shown in Figure 17.

The main drawback of this technology is the small etendue of the SMF (diameter 10 μm) and the related difficulty of injecting enough light into the cavity. To overcome this problem some instruments (Halverson et al. 2014) have adopted a supercontinuum, class IV laser, or as in our case, a Super-Luminescent Emitting Diode (SLED) that is a semi-conductor device emitting broadband light through electrical current injection. The intensity of the light from the SLED is tuneable and it is coupled to the FFP with a coaxial fiber connector. The tested prototype of FFP works in H band that is a typical wavelength range used in telecom industry. We utilized the SLED EXS210066-01 from EXALOS whose emission spectrum is shown in Figure 17. The procured prototype has a finesse $F = 276$, a signal attenuation of 2.2 dB and a FSR of 1 nm as shown in Figure 17. The FFP envisioned for the K band is conceptually the same of the development prototype, a SMF FFP coupled with a SLED. It is under development in collaboration with an external company for the

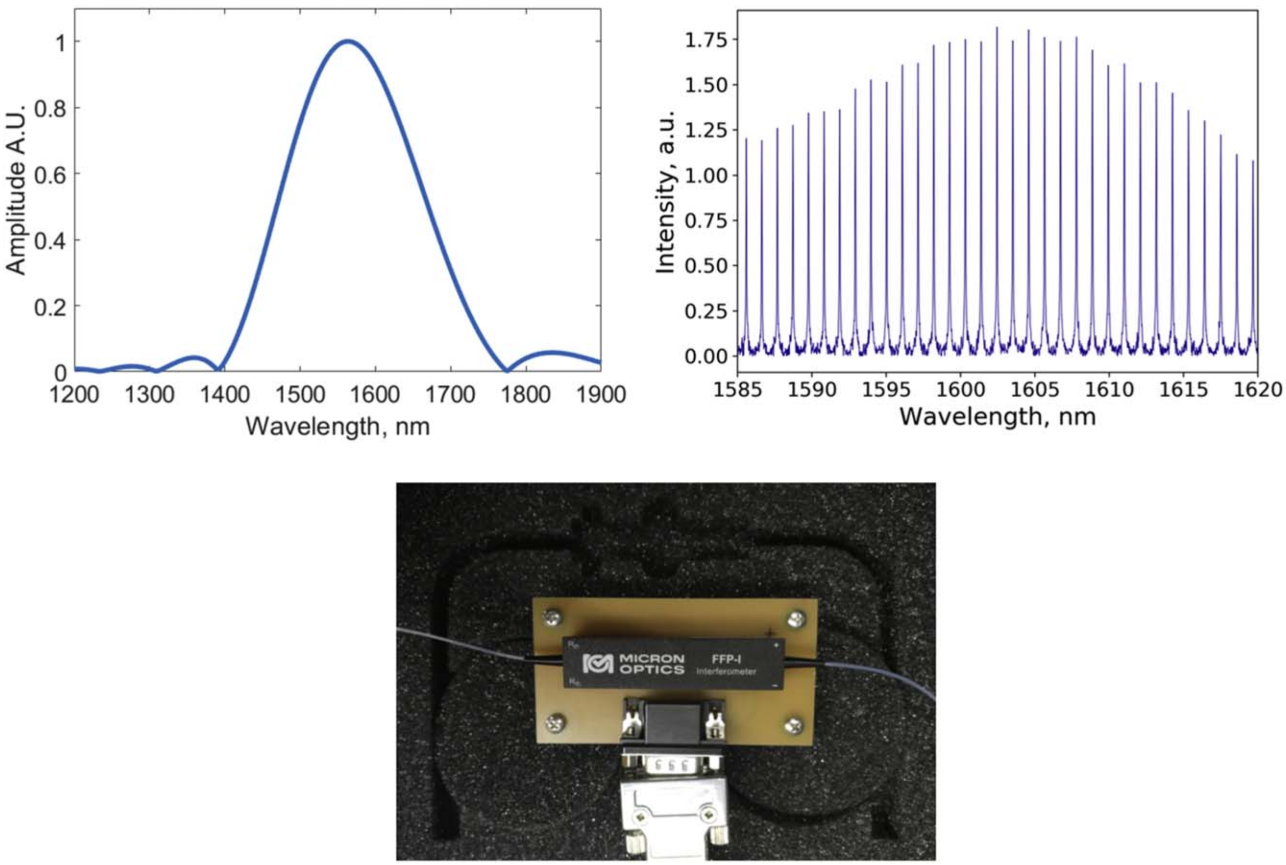

Figure 17. Top-left: spectrum of the SLED used as light source for the etalon Top-right: central part of the spectrum from the prototype etalon measured with the Nicolet iS50 Fourier transform spectrograph at a resolution $R \sim 100{,}000$; the free spectral range of 1 nm is clearly visible. Bottom: FFP based on a single mode fiber cavity with embedded thermoelectric cooler controller to stabilize its temperature.

(A color version of this figure is available in the online journal.)

fibres polishing and coating and with InnofSPEC (InnofSPEC 2020) for the alignment and assembly of the FFP. The K band FFP is realized using Z-BLAN glass fibres to ensure high throughput beyond $2\,\mu$m, and this collaboration opens to highly customized FFPs to fill other gaps in the spectrum if required by the scientific case. The FFP has the same opto-mechanical interface as the gas lamps to the FCU: an optical fiber brings the light from the FFP to the input port of the FCU where it impinges the Spectralon panel and it is diffused toward the spectrograph slit. A N-BK7 collimating lens, with transmission >99.9% in NIR, in front of the fiber concentrates the light from the gas lamps/FFP on the Spectralon in a pool that covers the size of the longest spectrograph slit as shown in Figure 18-bottom. Since the gas lamp flux cannot be tuned to a suitable value, the optical interface between with the FCU has to be optimized for minimizing the losses. Given the geometry of gas lamp, a cylindrical bulb 54 mm long with a diameter of 6.4 mm, the most efficient solution we envision is a fiber bundle with a rectangular input port (size 20 mm $\times$ 1.2 mm, see Figure 18-top) that covers a significant fraction of the bulb (∼40%). The fiber bundle collects 543 fibers of $200\,\mu$m diameter. The measured coupling efficiency is ∼26%.

5. FCU Wavelength S/N, RV Precision and Stability

Three quantities are of major importance for the development of a good wavelength calibration strategy: a suitable line density in the calibration source spectra, high S/N for at least 10 calibration lines (Kerber et al. 2008) (goal 30) for each order of the echellogram and the RV stability achievable with these calibration sources. The figure of merit of 10 lines for a given detector-spectrum order is proved by the experience with the X-shooter instrument that has a comparable resolution to MICADO in the NIR (Vernet et al. 2011). A simulation of the reliability of this assumption is shown in Figure 19.

The spectra from the gas lamps and the FFP have been studied to derive the above mentioned quantities using two Fourier Transform Spectrographs (FTS): a Bruker IFS 125HR and a Thermofisher iS50 Nicolet. The resolution of the iS50 Nicolet can be varied up to $R \sim 100{,}000$ in H band and it is

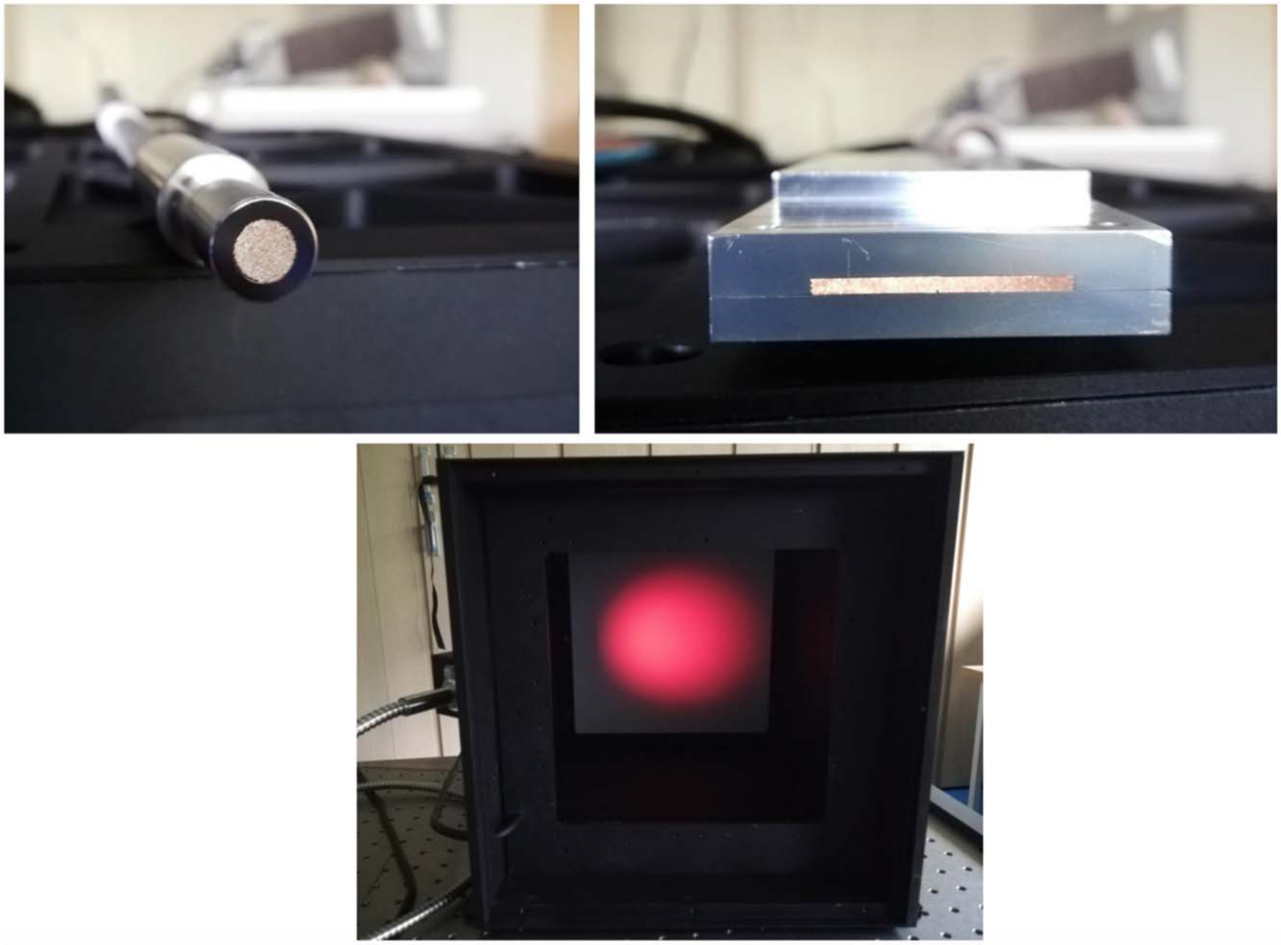

Figure 18. Top: view of the fiber bundle heads, the rectangular input port is the interface with the cylindrical gas lamp bulb, the output port reformats the bundle in a circle. Bottom: image of the FCU replica in reflection mode with the light pool from the gas lamp projected on the Spectralon panel over an area equivalent to the size of the longest MICADO spectrograph slit.
(A color version of this figure is available in the online journal.)

equipped with an InGaAs detector that provides high sensitivity in the NIR range. The light from the fibres is collimated using a refractive collimator and then injected into the FTS. Due to multiple reflections inside the FTS, the coupling efficiency and the intrinsic low efficiency of FTS spectroscopy, getting spectra with suitable S/N require a lot of scans (time) and it is intrinsically limited for faint lines. Another drawback of FTS spectroscopy is the uncalibrated flux in the measured spectra: what is conserved is the relative ratio between different lines in a certain spectrum, provided that the detector responsivity is removed, but the absolute flux of the lines is not directly measurable. The spectra of the four gas lamps (Ar, Kr, Xe, Ne) in the range 0.8–2.4 μm have been taken with the FTS at a resolution $R \sim 50{,}000$. The lines have been extracted from the spectra and matched to existing lines catalog from (NIST 2020) and other NIR astronomical instruments (Ramsay et al. 2008). An estimate of the absolute flux of some spectral lines has been derived using the current measured with an InGaAs photodiode through a passband filter. The current signal from the photodiode has been distributed among the multiple lines falling into the filter (Figure 20-top) calculating the relative areas of each line in the FTS spectrum. The calculation has been repeated using the spectra taken with two FTSs and three different detectors to boost the statistics (Figure 20-bottom).

As requirement, the brightest lines from the gas lamps shall reach a S/N of 200 within an exposure time of 30 s. We used a Zemax non-sequential design to propagate the absolute flux estimate from the lamp bulb to the FCU and through MAORY (7 surfaces) (Lombini et al. 2019) and MICADO (15 surfaces) downward to the instrument focal plane. The S/N estimates (see Equation (4)) for a faint and a bright line for each gas lamp are collected in Table 1.

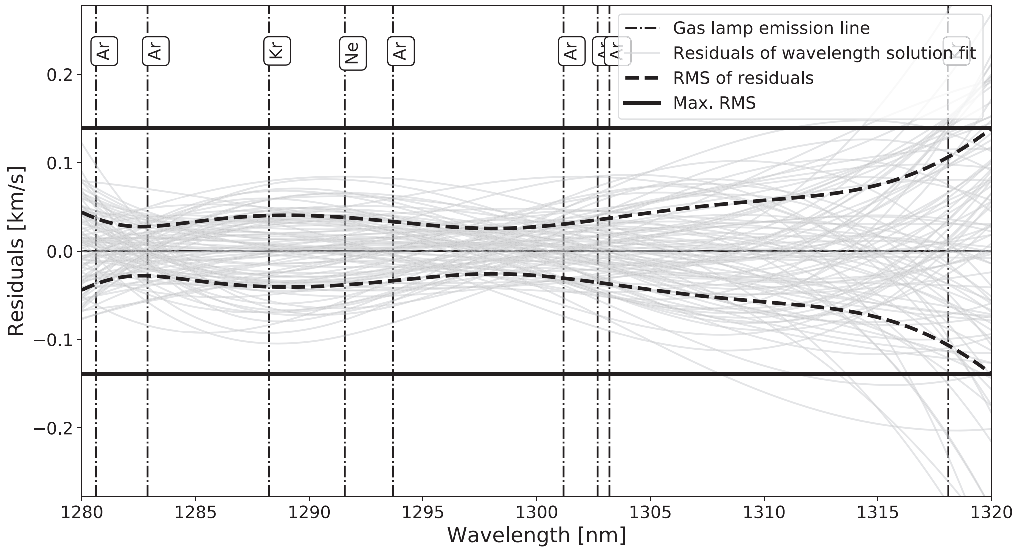

Figure 19. Simulated RV residuals (3rd order polynomial fit) for a segment of spectrum order falling within one detector. The fit is performed over nine gas lamps lines and leads to retrieve a maximum RV residual rms of 0.32 km s^{-1} in compliance with the FCU RV requirement. The rms residual is caused only by the polynomial fit numerical noise of otherwise ideal and stable theoretical lines.

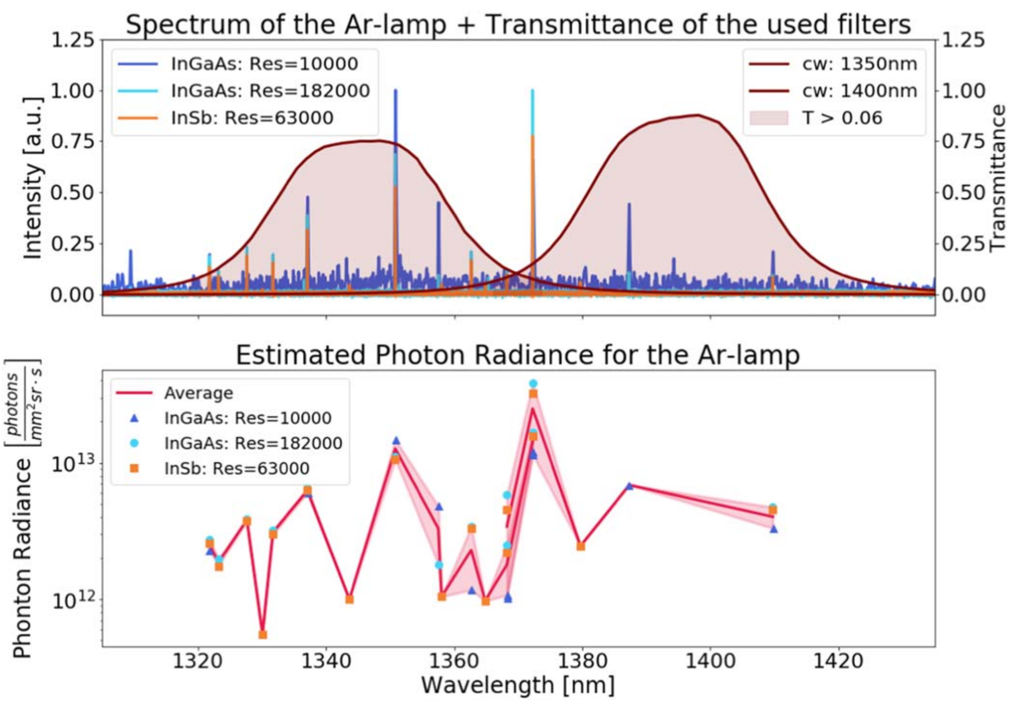

Figure 20. Example of Ar lamp absolute line flux estimate: the amplitude of some spectral lines isolated with a passband filter from the FTS spectrum (top) are converted in an absolute flux estimate by the measurement of the photocurrent detected with an InGaAs photodiode (bottom). The measurement taken with the InGaAs detector at $R = 10{,}000$ (blue line) is more noisy since the detector was not cooled.

(A color version of this figure is available in the online journal.)

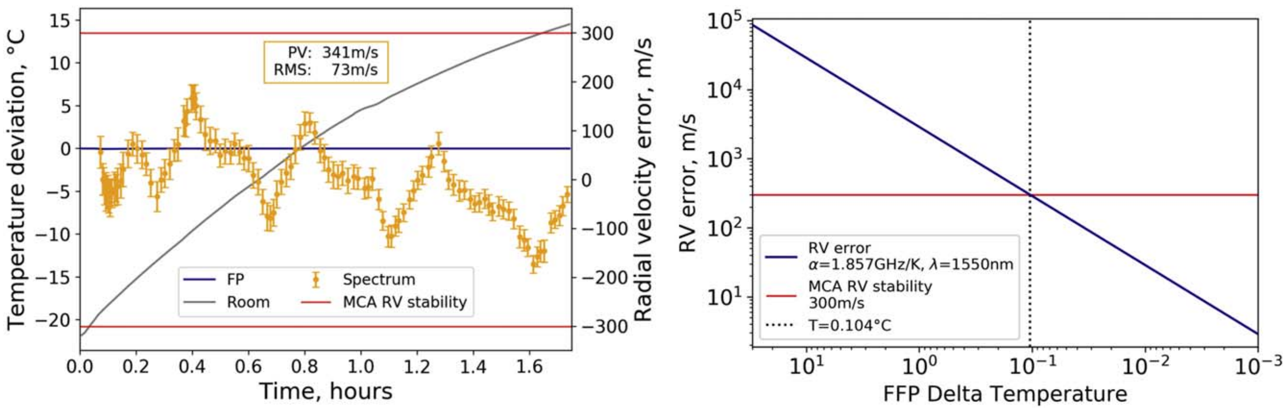

Figure 21. Left: measured RV stability of the FFP during a thermal test spanning a wide temperature range; the rms RV stability is 0.073 km s^{-1} with in closed-loop of the TEC. Right: estimated RV stability for different closed-loop temperature residual drifts; for the MICADO application a residual $\Delta T \sim 0.1$ K is enough to ensure an adequate RV stability of the calibration.

(A color version of this figure is available in the online journal.)

While the gas lamps lines have an absolute rest-wavelength position, the FFP lines move when the cavity temperature varies. A significant effort has been put on studying its thermal behavior and the stability of its spectrum against environmental temperature changes. The FFP cavity is made of glass and it is stabilized by the TEC connected to a LakeShore 336 temperature controller. We estimated the coefficient of thermal expansion α of the cavity by setting the TEC at a series of increasing temperature steps while measuring the wavelength shift of the line comb. The measured value is $\alpha \sim 1.857 \pm 0.001$ GHz K^{-1} and this translates to a spectrum wavelength shift $\Delta\lambda$and RV systematic error $\sigma_{\rm RV}$ regulated by Equation (5).

$$\Delta\lambda = \alpha \cdot \frac{\lambda^2 \cdot \Delta T}{c}\ \sigma_{\rm RV} = \frac{\Delta\lambda}{\lambda} \cdot c. \qquad (5)$$

The ability of the TEC in stabilizing the FFP determines the RV error as shown in Figure 21-right. The measured closed-loop temperature residual is $\Delta T \sim 1$ mK that corresponds to a RV residual $\Delta v \sim 3$ m s^{-1} while the achievable RV resolution with the MICADO spectrograph is $\Delta v_{\rm RV} \sim c/R \sim$ 20–30 km s^{-1}. To obtain a reliable calibration, the ratio between the FFP RV residual and the spectrograph resolution should be $\sigma_{\rm RV}/\Delta v_{\rm RV} \sim 10^{-1,\,-2}$. The thermal stability of the FFP has to be guaranteed within the temperature operational range for the ELT instruments (0, +15 °C). To assess this capability we performed a thermal cycle on a wider range (−20,+15 °C) acquiring periodic spectra of the FFP during the warm-up cycle and measuring the drift of its line comb with time. In this test the FFP temperature was set to a fixed value (+35 °C) and kept stable by the TEC against the external thermal gradient. The assessed RV residuals are $\sigma_{\rm RV} \sim 0.073$ km s^{-1} rms and $\sigma_{\rm RV} \sim 0.341$ km s^{-1} *PV* confirming that FCU can provide a signal within the MICADO calibration requirements of ± 0.3 km s^{-1} as shown in Figure 21-left.

Table 1
S/N Estimate of a Gas Lamp Bright and Faint Line for a 30 s Calibration Exposure Through the Different MICADO Spectrograph Slits

Gas Lamp	$\lambda_{\rm air}$, nm	S/N$_{s1}$	S/N$_{s2}$	S/N$_{s3}$
Ne	837.99	2724 ± 52	1104 ± 33	1781 ± 42
Ne	865.79	495 ± 22	199 ± 14	323 ± 18
Ar	1337.08	2149 ± 41	1232 ± 17	1987 ± 27
Ar	1330.05	642 ± 25	368 ± 19	593 ± 24
Kr	1689.51	4373 ± 679	1773 ± 275	2859 ± 444
Kr	1700.02	457 ± 21	184 ± 14	298 ± 17
Xe	1473.68	1183 ± 60	479 ± 24	773 ± 39
Xe	1223.86	247 ± 16	98 ± 10	160 ± 13

Note. The associate uncertainty on the S/N for the lines measured with more than one FTS is the *PV* of the measurements; for the lines with one single measurement is the Poissonian noise.

In the final MCA configuration all the spectral calibration sources will be installed in the electronic cabinets of the instrument and their light fiber fed to MICADO, as previously implemented in the PMAS-Calibration Unit (Roth et al. 2005) and the MUSE-CU (Kelz et al. 2012). With this arrangement the FFP will be in a controlled and stable environment in which the expected temperature variations will be significantly smaller than the operational and survival ranges mentioned above.

To have an indication of the improvement of the RV residual error when using a FFP in combination with the gas lamps, we simulate in a Montecarlo fashion the derivation of the wavelength solution with and without the FFP comb of lines. We consider the lines in a certain echelle order with their expected centroid uncertainties at the instrument focal plane and we create a set of

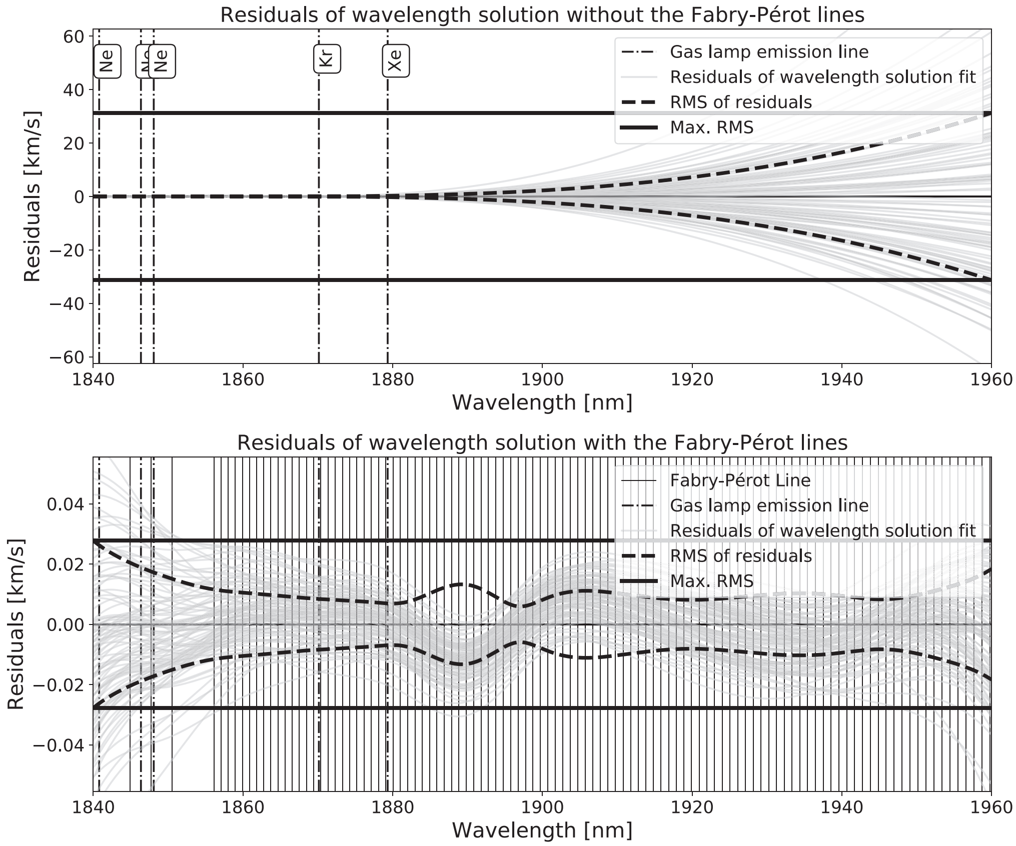

Figure 22. Simulated RV residuals of polynomial fit (3rd order) of the gas lamps (top) and the gas lamps combined with an FP operating in this wavelength range (1840–1960 nm). The maximum RV residual rms are 7.5 km s^{-1} (top) and 0.034 km s^{-1} (bottom).

spectra with randomized centroid uncertainties. A series of least-square fitting functions of different polynomial orders are then run on the spectra to determine their wavelength solution and the residual RV error. In regions of the spectrum were the gas lines are very rarefied (beyond 1.8 μm) the gain in RV residual when using a FFP in combination with the gas lines is quite evident as shown in Figure 22.

6. Simulating the Calibration Spectra

6.1. Input Creation and Setup

The MICADO focal plane incorporates an array of nine 4k × 4k-HAWAII-4RG detectors aligned in a 3 × 3 arrangement, which is fully covered by the current preliminary spectral order layout. We use the instrument simulator package SimCADOv0.6dev (Leschinski et al. 2016; Leschinski & Czoske 2018a) and its spectral subpackage SpecCADO v0.2.0 (Leschinski & Czoske 2018b) to get an impression on the resulting calibration spectra arising from the various lamps in the FCU. These simulated data are also the basis for the pipeline development and the testing of the MICADO specific reduction algorithms, which has to be done in parallel to the hardware development.

SimCADO contains the entire optical train including the Earth's atmosphere, the ELT mirrors, and the optical elements of MICADO. For the simulation of the calibration spectra from the FCU we need to restrict SimCADO to the relevant optically active components because the light from the FCU does not pass the entire Earth's atmosphere and the ELT optical system. We therefore removed the effects of the atmosphere above the telescope and all ELT mirrors. However, since there's an optical path of 26 m between the FCU and MICADO (see Section 1), which is exposed to air, we need to include the absorption arising from the molecules of the Earth's atmosphere in between. This absorption is mainly caused by the strong water vapor bands around 0.92 and 1.4 μm, and between 1.8 and 2.0 μm, respectively, but also arises from various other molecules like molecular oxygen (absorption band at ∼1.27 μm), carbon dioxide (several bands e.g., at ∼1.43, 1.6 μm, and ∼1.96, 2.01, 2.07 μm), and methane (several broader, but less dense and deep bands between 1.1 and 2.7 μm). It is important to take that absorption into account, because we need to estimate its influence on the

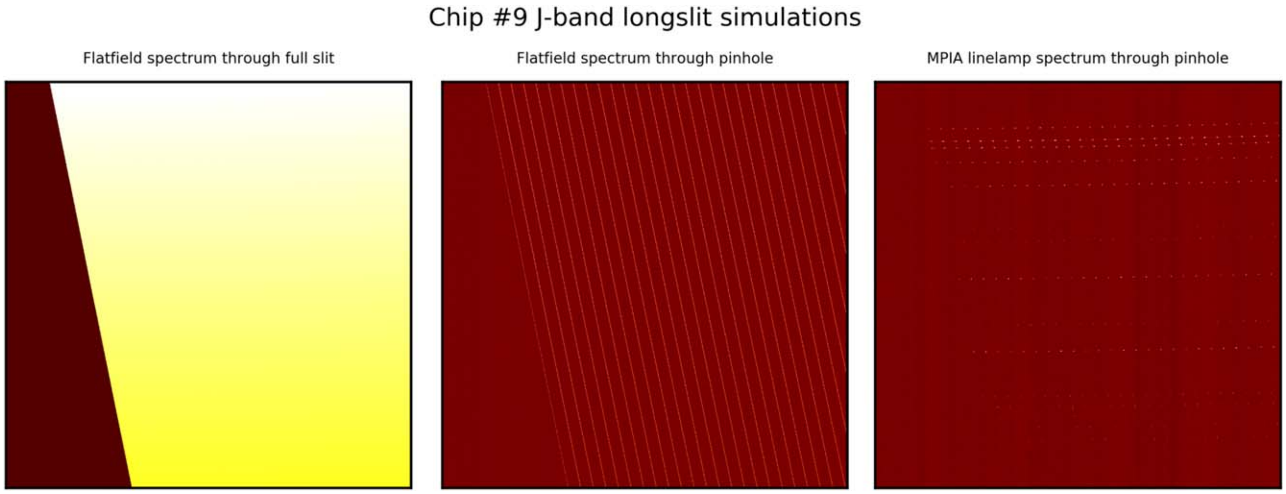

Figure 23. Comparison of the order o51 on Chip #9 in the *J*-longslit setup: left: simulated flat-field taken with the long slit in the *J*-band setup; middle + right: observations taken with the white light (middle) and the gas lamps (right) through the warm astrometric mask.
(A color version of this figure is available in the online journal.)

spectral flat-field and in particular the wavelength calibration lines over the entire 0.8–2.4 μm MICADO range to achieve a stable wavelength solution. To ensure the latter we have to know how many lines are affected by this internal absorption.

In order to calculate this MICADO internal absorption we use a special version of the ESO Paranal sky model code[6] (Noll et al. 2012; Jones et al. 2013). This model calculates a transmission by means of the line-by-line radiative transfer code `LBLRTM` (Clough et al. 2005), a molecular line list based on the HITRAN database (Rothman et al. 2009), and atmospheric data containing height profiles of temperature, pressure and various molecular species. To simulate a 26 m atmospheric profile we incorporate the major absorbing molecules described above, which are present in our Earth's atmosphere. We assume a constant concentration of these species for the 26 m length at the altitude of the ELT (3060 m a.s.l.), with a water vapor column density representative for a relative humidity value of 10%. Usually at Cerro Armazones the relative humidity is below that value, thus this can be assumed to represent an average lower limit of the observing ambient condition quality.

For the simulation of the FCU calibration lamps we need to create the input spectra required by SimCADO. The flat-field lamp is modeled as blackbody emitter with a temperature of $T = 1500$ K. This is a realistic estimate arising from Equation (2) for an intermediary value for the lamp voltage. For the simulation of the penray lamps and the FFP used for the wavelength calibration we created synthetic spectra by a Gaussian smoothing of the line lists derived from the gas lamps and the FFP (see Section 5). The Gaussian width was chosen to be $\sigma = 4 \cdot 10^{-5}$ μm, and the spectral sampling corresponds to a resolving power of $R = 40{,}000$ at 0.8 μm. This ensures to fulfill the Nyquist sampling criterion over the entire wavelength range to simulate the expected spectral MICADO resolution with SimCADO. The fluxes of all light sources and the exposure times were chosen to achieve a decent signal-to-noise level on the detectors. All calibration unit sources are assumed to uniformly fill the full slit and are therefore not point sources.

MICADO has two spectral setups for the short 3 as-slits covering the *IzJ*-band and the *HK*-band regimes, respectively. For the long 15 as slit, the spectral setup is restricted to the *J* and the *HK* bands to avoid lateral order overlaps on the FPA. As example for the order layout and the results Figure 24 shows the simulations of the wavelength calibration sources on the FPA in the *IzJ* regime calculated with the SimCADO package. For the time being we use the SpecCADO internal routine for the rectification, which provides a 2D spectrum in (x, λ) space by performing the inverse projection of the previous mapping of the slit (as seen on sky) toward the order layout on the FPA done in SimCADO.

Since the FPA consists of 3 × 3 HAWAII-4RG detectors, spectral gaps between the individual detectors are unavoidable. Thus, we also used an order layout shifted by 5 mm in the y-direction (realized by a second set of slits in the filter wheel) to be able to recover the spectrum arising from the horizontal gaps. This is sufficient since these gaps are only 2.4 mm wide (see Figure 24). A shift in x-direction to recover the missing vertical parts of the orders is neither desirable (loss of order information at the left/right FPA borders), nor required, because we intend to apply a nodding technique during observations, which places the scientific object at different positions along the slit anyway.We also simulate the benefit of extending the wavelength calibration strategy by including

[6] https://www.eso.org/sci/software/pipelines/skytools/skymodel

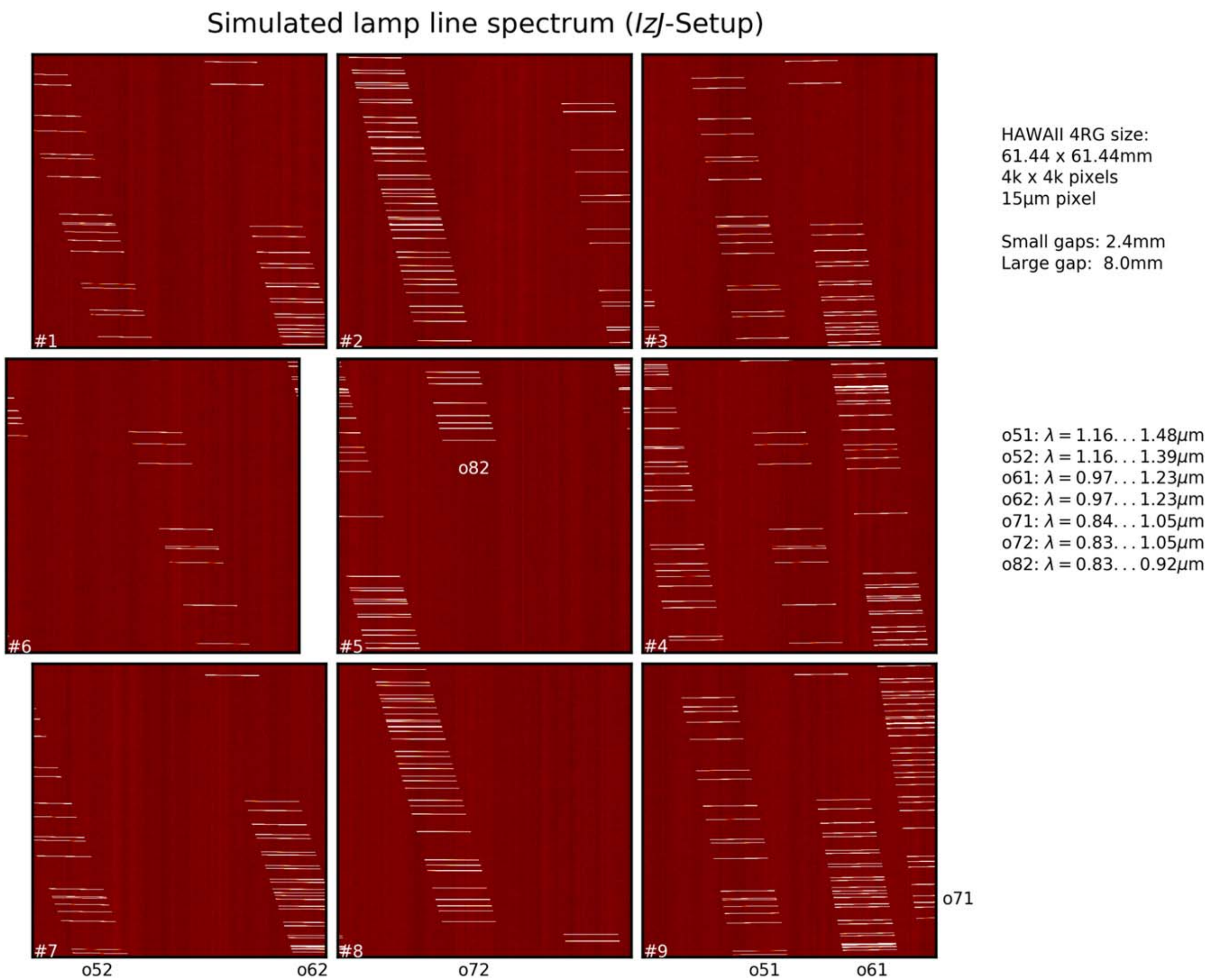

Figure 24. Simulation of the FCU wavelength source spectra incorporating the short 3 as × 16 mas-slit in the *IzJ*-setup on the 3 × 3 detector array. The labeling of the individual spectral orders denoted the order/crossorder selection, e.g., o51 denotes the order #5 of crossorder #1.The gap between detector #5 and #6 cannot be avoided since it is due to a wire bonds region that every HAWAII-4RG detector has on one side of the chip. All the other detectors in the FPA have the wire bonds region oriented toward the external side of the focal plane.

(A color version of this figure is available in the online journal.)

some functionalities of the MICADO Astrometric Calibration Unit (ACU) to trace the geometry of the echelle orders. In the specific, the ACU could provide a series of frames used for the order rectification. These frames are taken with the Warm Astrometric Mask (WAM) that is part of the ACU (Rodeghiero et al. 2019) and it provides a matrix of pinholes. In this calibration scenario, the WAM is back side illuminated and its image is relayed by the relay optics and projected on top of the slit, leading to several point-like sources along the slit. The reason is that -especially for the long slit observations- the orders are truncated by the FPA edges (see Figure 23 left), which leads to major problems for the rectification since one side of the trace cannot be reconstructed. The white light WAM pinholes frames provide well defined traces along the spatial direction, whereas adding four fiber bundles to the ACU collecting the light from the same gas lamps of the FCU would give well defined anchor points along the wavelength direction (see Figure 23 middle and right) for a reliable order reconstruction and rectification.

6.2. Simulation Results and Discussion

Figure 25 shows order #4 of crossorder #1 (abbreviated by "o41") of the *HK*-setup in detail. It covers the wavelength range $\lambda = 1.45....1.85$ μm. In panel (a) the list consisting of the XeArNeKr-gas lamps and the FFP spectral lines is shown, the

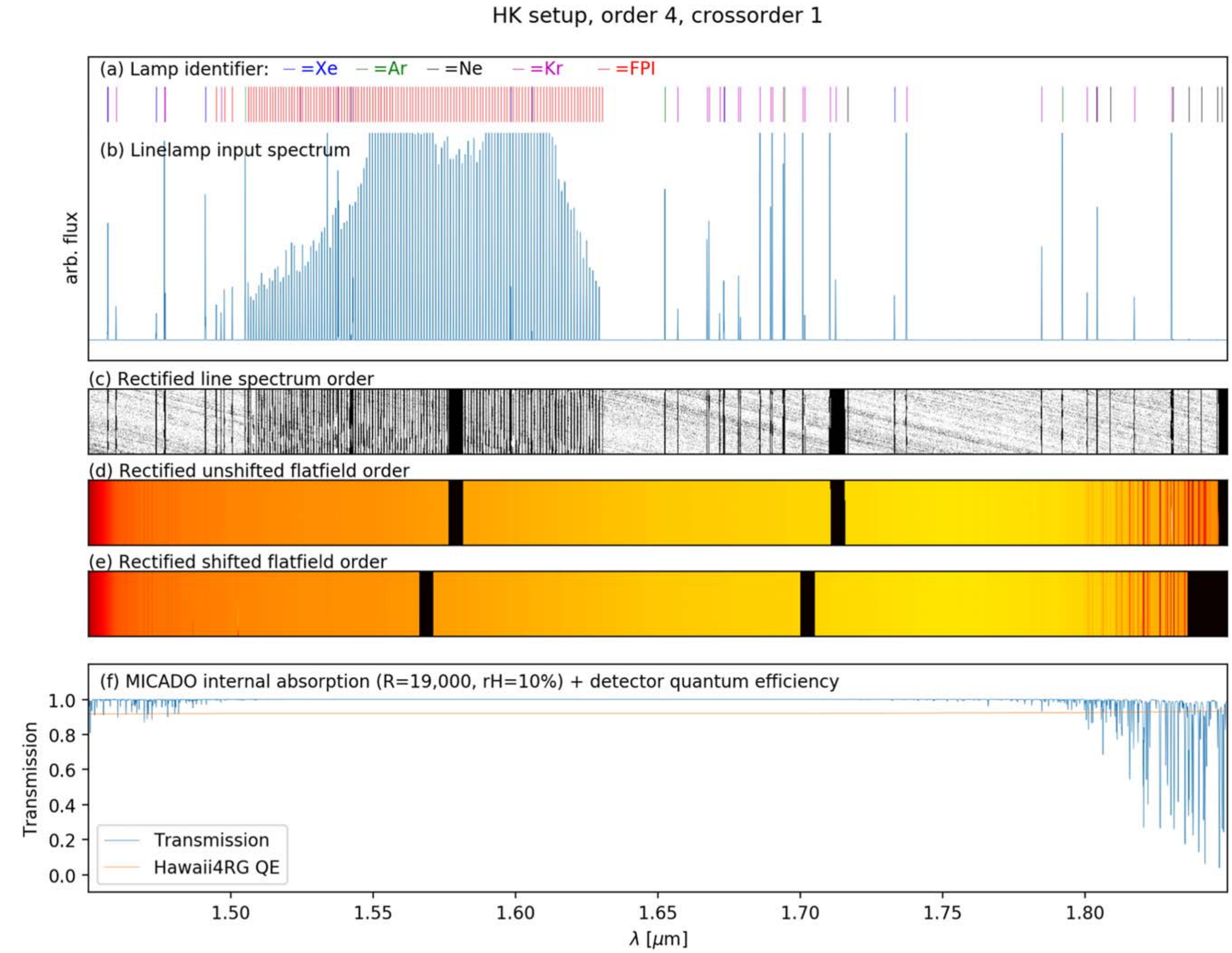

Figure 25. Example of a simulated *HK* order (wavelength range $\lambda = 1.45 \ldots 1.85\ \mu$m) including (a) the input sources (XeArNeKr-gas lamps and the FFP), (b) the resulting input spectrum, (c) the rectified order showing the line spectrum and the flat-field spectrum ((d) unshifted and (e) shifted), and (f) the MICADO internal transmission in that wavelength regime of this order.
(A color version of this figure is available in the online journal.)

resulting Gaussian smoothed spectrum, which is used as input for SimCADO, is given directly below in panel (b). The gray-scaled panel (c) is the rectified order o41 and clearly shows the individual lines from the calibration lamps and the spectral gaps arising from the detector interspaces. The two panels (d) and (e) show the rectified order o41 for the flat-field lamp, both for the unshifted and shifted order layout, respectively. The gaps are shifted by $\lambda \sim 10.5$ nm in wavelength direction (i.e., 5 mm in the FPA), which offers enough overlap to fully recovery of the gap losses. In the flat-field spectra also absorption features arising from the atmospheric molecular absorption along the light path between the FCU and the MICADO instrument are clearly visible at the red end. Panel (f) shows the MICADO internal absorption together with the detector quantum efficiency for comparison.

The investigation of the MICADO internal absorption effects revealed that it can be very prominent in certain wavelength ranges (e.g., the longer wavelength part of Figure 25), but affecting only minor parts of the orders. Since there is no total absorption, only a few calibration lines are attenuated to a certain degree but are still visible, we therefore conclude that, under the assumed conditions, the loss of calibration lines is negligible. The internal absorption however does also affect the flat-field spectra (see Figure 25). It is currently under investigation whether we need to correct for that effect, e.g., by interpolating these bands with a BB model.

We also investigated the line density per order to check whether the number of anchor points is sufficient for a decent wavelength calibration. The majority of the spectral range is well covered, except some regions, e.g., around ∼1.01....1.2 μm or in the *HK* regime, where only some weak gas lamp lines are visible. We therefore investigate the supplement with further FFPs as described in Section 5 and/or the usage of atmospheric OH airglow lines as additional reference frame.

7. Conclusions

This paper reports the evolution of the MICADO flat-field and wavelength calibration unit from the early beginning until its final design. The calibration unit architecture presents many novelties with respect to the past and current astronomical instruments. The linear size of the MICADO focal plane and of the ELT pose many challenges to the use of conventional integrating spheres or telescope dome for the flat-field illumination and require a completely new approach using a single scattering surface either in reflection or transmission, fully tested against the system requirements. The FCU performances on the flat-field global and local uniformity have been assessed for both the FCU modes (reflecting and transmitting), Section 3.1, showing compliancy with the uniformity requirements exception made for a uncritical non-uniformity for the transmitting mode at 0.3% level (requirement 99.9%). The FCU can provide flat-field calibration frames with a suitable S/N within 2 s exposure for all the MICADO filters exploiting two illumination levels depending on the bandwidth of the filter (3.2). The absolute flux measurements with two InGaAs photodiodes assessed the ability of the FCU to cover among 1% and 90% of the detector dynamic range, thus enabling to investigate the nonlinearity effect at low illumination levels. The combination of the detector plane segmentation in 3×3 elements and the intrinsically low density of gas lamp calibration lines beyond 1.8 μm makes the absolute wavelength calibration challenging. A test campaign on the gas lamp for the NIR using two FTSs led to a lines census assessing the compliancy with the requirement on the numbers of lines per oder and detector and the RV precision of the wavelength solution (4). The lack of natural lines in *K* band has been overcome with the adoption of a FFP. A pilot study on the stability of this device has been carried out on an *H* band prototype and the acquired knowledge is now driving the development of the *K* band FFP. The measured calibration lines data set has been used to develop part of the MICADO instrument simulator and to assess the accuracy of the expected wavelength solution. The simulation results has underlined also some possible strengthening of the calibration pipeline if the ACU is used to trace the geometry of the echelle orders.

Authors are grateful to the anonymus referee for the suggested corrections and ameliorations to the manuscript. Authors would like to thank Uwe Hassdenteufel from MGG, Jürgen Bitterlich, Michael Schröder and Bruno Beccard from Thermofisher. Thanks to Florian Kerber for the support in the test of the flat-field membrane at Paranal and to Maximilian Fabricius and Frank Grupp for the useful discussion on the FFP development and the MICADO spectrograph design.

ORCID iDs

Gabriele Rodeghiero https://orcid.org/0000-0002-3469-9863
Maximilian Häberle https://orcid.org/0000-0002-5844-4443
Jörg-Uwe Pott https://orcid.org/0000-0003-4291-2078
Wolfgang Kausch https://orcid.org/0000-0003-3557-7689

References

Bhandari, A., Hamre, B., Frette, Ø., et al. 2011, ApOpt, 50, 2431
Boggio, J. M. C., Fremberg, T., Bodenmller, D., et al. 2012, Proc. SPIE, 8450, 84501H
Chromey, F. R., & Hasselbacher, D. A. 1996, PASP, 108, 944
Clénet, Y., Buey, T., Gendron, E., et al. 2018, Proc. SPIE, 10703, 1070313
Clough, S. A., Shephard, M. W., Mlawer, E. J., et al. 2005, JQSRT, 91, 233
Davies, R., Alves, J., Clénet, Y., et al. 2018, Proc. SPIE, 10702, 107021S
Diolaiti, E., Arcidiacono, C., Bregoli, G., et al. 2014, Proc. SPIE, 9148, 91480Y
Hall, D. N. B., Atkinson, D., Blank, R., et al. 2016, Proc. SPIE, 9915, 99150W
Halverson, S., Mahadevan, S., Ramsey, L., et al. 2014, PASP, 126, 445
Hänsch, T. W. 2006, RvMP, 78, 1297
Huke, P., Schäfer, S., Reiners, A., et al. 2018, Proc. SPIE, 10702, 107029L
InnofSPEC 2020, Innovative faseroptische Spektroskopie und Sensorik, https://innofspec.de/en/
Jones, A., Noll, S., Kausch, W., Szyszka, C., & Kimeswenger, S. 2013, A&A, 560, A91
Kelz, A., Bauer, S.-M., Hahn, T., et al. 2012, Proc. SPIE, 8446, 84465T
Kerber, F., Saitta, F., Bristow, P., & Vernet, J. 2008, Proc. SPIE, 7014, 70143Y
Labsphere 2017, Integrating Sphere Theory and Applications, http://www.labsphere.com
Leschinski, K., & Czoske, O. 2018a, SimCADO v0.7, https://simcado.readthedocs.io/en/latest/index.html
Leschinski, K., & Czoske, O. 2018b, SpecCADO v0.2.0, https://github.com/oczoske/SpecCADO
Leschinski, K., Czoske, O., Köhler, R., et al. 2016, Proc. SPIE, 9911, 991124
Lombini, M., Diolaiti, E., & Patti, M. 2019, MNRAS, 486, 320
Loose, M., Beletic, J., Garnett, J., & Xu, M. 2007, Proc. SPIE, 6690, 66900C
NIST 2020, National Institute of Standards and Technology, https://www.nist.gov/
Noll, S., Kausch, W., Barden, M., et al. 2012, A&A, 543, A92
Photonics 2020, Integrating Spheres: Collecting and Uniformly Distributing Light, https://www.photonics.com
Ramsay, S. K., Rolt, S., Sharples, R. M., & Davies, R. 2008, in 2007 ESO Instrument Calibration Workshop, ed. A. Kaufer & F. Kerber (Berlin: Springer), 319, doi:10.1007/978-3-540-76963-7_43
Rico, G. D., Dolci, M., Valentini, G., & Cantiello, M. 2012, Proc. SPIE, 8446, 844641
Rodeghiero, G., Pott, J.-U., Münch, N., et al. 2018, Proc. SPIE, 10702, 107028U
Rodeghiero, G., Sawczuck, M., Pott, J.-U., et al. 2019, PASP, 131, 054503
Roth, M. M., Kelz, A., Fechner, T., et al. 2005, PASP, 117, 620
Rothman, L. S., et al. 2009, JQSRT, 110, 533

Schäfer, S., Guenther, E. W., Reiners, A., et al. 2018, Proc. SPIE, 10702, 1070276

Schubert, J., Hartl, M., Hrmann, V., et al. 2018, Proc. SPIE, 10702, 107028W

Seemann, U., Anglada-Escude, G., Baade, D., et al. 2014, Proc. SPIE, 9147, 91475G

te Plate, M., Holota, W., Posselt, W., et al. 2005, Proc. SPIE, 5904, 185

Verdoes Kleijn, G. A., Kuijken, K. H., Valentijn, E. A., et al. 2013, ExA, 35, 103

Vernet, J., Dekker, H., D'Odorico, S., et al. 2011, A&A, 536, A105

Wei, P., Shang, Z., Ma, B., et al. 2014, Proc. SPIE, 9149, 91492H

Wildi, F., Mouillet, D., Beuzit, J.-L., et al. 2009, Proc. SPIE, 7440, 74400Q